MICHIGAN STATE UNIVERSITY

CYCLOTRON LABORATORY

PRECOMPOUND EMISSION OF LIGHT PARTICLES IN THE REACTION $^{16}O + ^{238}U$ AT 20 MeV/u

T.C. AWES, G. POGGI, C.K. GELBKE, B.B. BACK,
B.G. GLAGOLA, H. BREUER, and V.E. VIOLA, JR.

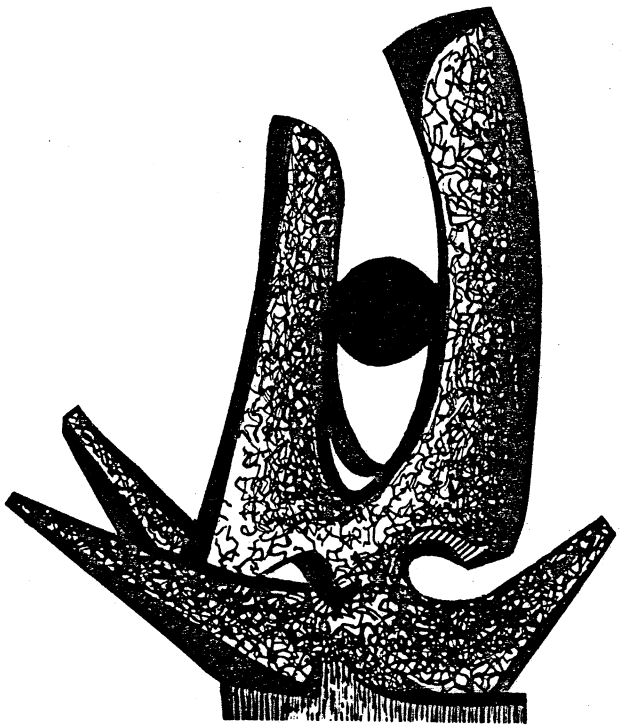

DECEMBER 1980

MSUCL-343

MSUCL-343
December 1980

Precompound Emission of Light Particles in the Reaction $^{16}O + ^{238}U$ at 20 MeV/u

T.C. Awes, G. Poggi[+], and C.K. Gelbke[++]

Cyclotron Laboratory, Michigan State University
East Lansing, Michigan 48824

B.B. Back and B. G. Glagola

Chemistry Division, Argonne National Laboratory
Argonne, Illinois 60439

H. Breuer and V.E. Viola, Jr.[+++]

Departments of Physics and Chemistry
University of Maryland, College Park, Maryland 20742

[+]On leave from the University of Florence, Italy

[++]Alfred P. Sloan Fellow

[+++]John Simon Guggenheim Fellow, present address:
Department of Chemistry, Indiana University,
Bloomington, Indiana 47401

ABSTRACT

Double differential cross sections have been measured for energetic p, d, t and α particles emitted in reactions of 315 MeV ^{16}O ions on ^{238}U. In coincidence with light-particle emission the momentum transfer to the target is determined by measuring the folding angle between the two fission fragments resulting from the sequential decay of the target nucleus. It is concluded that the emission of these particles occurs predominantly in fusion-type "central" collisions and at an early stage of the reaction. The energy and angular distributions are described by thermal emission from a source moving with approximately half of the beam velocity. Alternatively, the energy spectra can be explained by emission from a rotating hot spot.

The cross sections for d, t and α emission can be described in terms of a generalized form of the coalescence model which takes into account the Coulomb repulsion from the target nucleus.

I. INTRODUCTION

The emission of light particles in heavy-ion-induced reactions contains important information about the reaction mechanism. At low energies ($E/A \lesssim 5$ MeV/u above the Coulomb barrier) there is clear experimental evidence[1-4] that the majority of light particles are due to thermal emission from the compound nucleus or from fully accelerated and equilibrated fragments. On the other hand, non-equilibrium emission of light particles has been observed[5-24] for reactions induced by lighter projectiles ($A \approx 16$) and at higher energies ($E/A \gtrsim 8$ MeV). Originally, the energetic light particles that were observed in these experiments were associated with projectile breakup reactions[5]. However, subsequent coincidence experiments have demonstrated[10,12,15-20,22] that reactions where the major part of the projectile is absorbed by the target nucleus make an important contribution to the emission of light particles. These reactions have been variously termed as "incomplete fusion"[18] or "massive transfer"[15,16] reactions or "central"[17] collisions.

Several possible mechanisms have been proposed to explain the emission of non-compound energetic light particles. In qualitative terms, it has been suggested[15-18] that energetic light particles are emitted in a transfer or projectile breakup process where the larger fraction of the projectile mass is absorbed by the target nucleus. On a more quantitative basis, the possible formation of a "hot spot", i.e. a locally heated region of the nucleus, has been suggested[8,14,25-27]. Such a "hot spot" could attain much higher temperatures than the compound nucleus. Immediately after its formation, the

hot spot would cool by thermal diffusion into the adjacent cold nuclear matter or by the emission of energetic light particles. The predicted energy spectra exhibit exponential slopes that correspond to significantly higher temperatures than the compound nucleus temperature. Rather good agreement with experimental data has been obtained in several examples[26]. In addition to an interpretation in terms of the "hot spot" model, several features of the single-particle inclusive cross sections could be explained[6,23] in terms of preequilibrium[28-30] and intranuclear cascade[31] calculations. Furthermore, the prompt emission of light particles[32,33] ("PEPs"), and the enhanced alpha-particle emission[34] from superdeformed nuclei have been proposed as additional reaction mechanisms that could produce energetic light particles in the exit channel.

Up to now, most of the experimental effort has been devoted to coincidence studies which were designed to elucidate certain aspects of the emission of precompound light particles. These experiments are generally very phase space selective and the resulting cross sections are difficult to connect to the single-particle inclusive cross sections. On the other hand, most of the theories developed up to now have been formulated to predict single-particle inclusive cross sections. As a consequence, these theories could not be subjected to sufficiently stringent tests that could help differentiate between the various models.

In the present paper we present a study of the emission of energetic light particles (p, d, t, α) detected in coincidence with

two fission fragments resulting from ^{16}O-induced reactions on a ^{238}U target at an incident energy of 315 MeV. It is very likely that the simple requirement of two coincident fission fragments imposes only minor phase space restrictions, since only the most quasi-elastic collisions will lead to exit channels that do not result in fission of the target residue. On the other hand, by employing the correlated fission fragment technique[17,35,36] valuable information on the momentum transfer to the target residue is obtained. This allows a discrimination between "peripheral" collisions, such as inelastic scattering, breakup or transfer reactions, and "central" collisions, such as massive transfer, complete and incomplete fusion. It should, therefore, be possible to use the present results as a test case for the various theories that have been put forward. At the same time one can arrive at some qualitative conclusions that should yield useful information for the improvement of the various models.

The paper is organized as follows: The experimental details are given in section II. The relative contributions of "peripheral" and "central" collisions to the emission of energetic light particles are discussed in section III. A comparison of proton energy spectra observed for these two classes of reactions is given in this section. In section IV we discuss the light-particle energy spectra in terms of a rotating hot spot model[14,20] and in terms of a thermal spectrum observed in a frame of reference that moves with a velocity intermediate between those of target and projectile. In section V, the connection between the cross sections for the emission of protons, deuterons, tritons and alpha particles will be discussed and the validity of a generalized coalescence relation

will be demonstrated. A summary of our conclusions will be given in section VI. Some of the present results have been published in a previous letter[24].

II. EXPERIMENTAL TECHNIQUE

The experiment was performed at the 88-inch cyclotron of the Lawrence Berkeley Laboratory. A self-supporting metallic ^{238}U target of approximately 500 $\mu g/cm^2$ areal density was bombarded by $^{16}O^{6+}$ ions at 315 MeV with a beam current of ~20 nA.

A. Detection System

A schematic drawing of the experimental layout is shown in Fig. 1 . It consisted of four $\Delta E - E$ light-particle telescopes mounted in the plane of two position-sensitive fission detectors. All detectors were mounted on a movable table inside the scattering chamber. Two experimental geometries were used. In geometry I, the light-particle telescopes were placed at the scattering angles of -95°, -25°, 70°, and 140°; they subtended solid angles of 49, 23, 24, and 59 msr respectively. The position-sensitive detectors were located at $\theta_A^\circ = -60^\circ$ and $\theta_B^\circ = 100^\circ$, subtending an angular range of about ±20°. For geometry II, the entire arrangement was rotated by -15° to give four additional angles (-110°, -40°, 55°, 125°) for light-particle observation. Accordingly, the fission detectors were then centered at $\theta_A^\circ = -75$ and $\theta_B^\circ = 85$. In geometry I, one telescope was moved for a portion of the run to the forward angle of 15° subtending a solid angle of 15 msr.

The four $\Delta E - E$ telescopes each consisted of a 400 μm surface barrier Si detector and a 3"-thick NaI detector. Energy signals for the NaI detectors were typically taken from the fifth dynode of the photomultiplier tube. For hydrogen isotopes the energy calibration of the NaI detectors was established by measuring the

elastic scattering of protons on a ^{197}Au target at incident energies of 20 MeV and 45 MeV. Due to long-term drifts of the NaI detectors, the accuracy of this energy calibration is about 3%. For the response of the NaI detectors to alpha particles an independent energy calibration was established. This was necessary because these detectors displayed rather large pulse height defects and non-linearities. The energy calibration for alpha particles was obtained by measuring the elastic scattering of alpha particles on a ^{197}Au target at 80 MeV. This gave a fixed point for the calibration. The energy deposited in the ΔE detector was then used to determine the thickness of the ΔE detector. The response of the NaI detector to alpha particles was then established from a continuum spectrum by setting gates on the ΔE signal and calculating[37] the alpha-particle energy corresponding to the measured ΔE signal. The overall accuracy of this procedure is about 5%.

The energy calibration of the ΔE silicon detectors was done by injecting a known amount of charge into the input stage of the detector preamplifiers. This calibration was verified by measuring the alpha-particle energy spectra resulting from the decay of ^{241}Am and ^{252}Cf. At the forward angle of 15° an aluminum absorber of .64 mm thickness was placed in front of the telescope to prevent pile-up and radiation damage in the ΔE detector by the high flux of elastically scattered ^{16}O nuclei.

The energy calibration of the two position-sensitive fission detectors was established by measuring the energy spectra of the fission fragments resulting from the spontaneous decay of ^{252}Cf

and then using the Schmitt[38] calibration procedure. The position calibration was obtained by viewing a ^{252}Cf source through a mask with 15 equally spaced slits of 0.8 mm width placed over each detector. This calibration gave an angular resolution for the detectors of ± 0.3 degrees. Since the detectors were mounted close to the target, the angular calibration of the fission detectors was quite sensitive to uncertainties in the exact beam and target position. To minimize systematic errors we have measured the folding-angle distribution for four different target positions. This allows measurement of and, when necessary, correction for the effects of small misalignments of beam and target with respect to the center of the scattering chamber[36]. It is estimated that the fission fragment folding angle, θ_{AB}, is measured with an overall accuracy of $\Delta\theta_{AB} \sim 1°$.

B. Data Acquisition and Reduction

The raw data were recorded event by event on magnetic tape using the LBL Modcomp computer system. Sixteen parameters were recorded on tape: the energy signals of all ten detectors, the two position-dependent signals of the position sensitive fission detectors, and the four timing signals corresponding to the time separation between fission detector A and the four light-particle telescopes. In addition the coincidence time signal between the two fission detectors was monitored and used to gate the computer to ensure that two fission fragments were detected for each event. Since only a negligible number of random coincidences between the

two fission detectors were observed ($\sim 10^4$ real-to-random ratio), this parameter was not recorded on tape.

A "coincidence event" was defined as a coincidence between the two fission fragments and at least one of the light-particle telescopes. In addition to coincidence events, "inclusive fission events" were recorded on tape at a downscaled rate for normalization purposes. An inclusive fission event was defined as a coincidence between two fission fragments.

Mass and charge identification of the light particles was obtained by using a standard particle identification function of the form[39]

$$P.I. \propto (E + \Delta E)^{\gamma} - E^{\gamma} \qquad (1)$$

where ΔE and E denote the energies deposited in the ΔE and E detectors and γ is a parameter which varied from 1.6 to 1.8. In the analysis, a contribution of approximately 10% ^3He was included in the ^4He spectra.

C. Normalizations

The fission fragment folding-angle distributions, θ_{AB}, have been corrected for the geometrical efficiency of the fission detection system. The coincident light-particle spectra were also corrected for the fission detection efficiency on an event by event basis. The detection efficiency, shown in Fig. 2, was determined by a computer simulation of the fission decay of ^{254}Fm.

In these simulations we assumed that the total momentum vector of the recoiling ^{254}Fm nucleus was directed parallel to the beam axis. This assumption is necessarily fulfilled for compound nucleus reactions. For more peripheral reactions, on the other hand, the momentum components perpendicular to the beam axis could be appreciable. In that case, the momentum vectors of the fission fragments could span a plane that does not contain the beam axis and our calculations would overestimate the detection efficiency. In other words, the experimental requirement of the detection of two fission fragments that are emitted in a plane that contains the beam axis might reduce the detection efficiency for reactions involving appreciable transverse momentum transfers. Since the transverse momentum distribution of the target residue is not known, these effects could not be corrected for. The coincident light-particle cross sections are presented as the number of light particles normalized to the number of inclusive fission events N_f.

III. EXPERIMENTAL RESULTS

A. Fission Fragment Folding-Angle Distributions

The fission fragment folding angle, θ_{AB}, is defined as the angle of emission between two coincident fission fragments measured in the laboratory system. The folding angle has been shown[17,36] to be mainly determined by the projection, $P_R^{\parallel}$, of the target recoil momentum onto the beam axis. In Fig. 3, this relationship is shown for average values of θ_{AB} which have been calculated by computer simulation assuming fission of either ^{238}U or ^{254}Fm nuclei moving parallel to the beam axis. The relationship is approximately linear for the average folding angle. In practice, there will be a distribution of folding angles corresponding to a given recoil momentum. This is partially due to the distribution of fission momenta which results from the fission fragment mass distribution. It is also due to neutron evaporation from the fission fragments. The dependence of the folding angle on the mass of the fissioning nucleus is shown for both fission detector geometries used in the present study. The two curves for each geometry provide limiting cases of the actual relationship expected. The curve for the fission of ^{254}Fm will be valid for the case of complete fusion of target and projectile ($P_R^{\parallel} = P_1$, where P_1 is the beam momentum), and the ^{238}U curve will hold in the event that no mass is transferred to the target. Consequently, the curve for ^{254}Fm will be more realistic for large momentum transfers, whereas the curve for ^{238}U will be more realistic for small momentum transfers. The simulation of the different experimental geometries predicts

a shift of approximately 2° in the region of full momentum transfer when going from the more symmetric geometry II to the less symmetric geometry I.

1. Inclusive Folding-Angle Distributions

The distributions of fission fragment folding angles measured for inclusive fission events is shown in Fig. 4. The distributions are shown for the two fission detector geometries of the present experiment and also for the geometry of a previous experiment[17,36] ($\theta_A^o = -\theta_B^o = 80°$). The inclusive distributions exhibit two clearly distinct components. The strongest component centered in the region of $\theta_{AB} \simeq 150°$ corresponds to large recoil momenta (see Fig. 3). We will define these reactions (which can be associated with fusion, "incomplete fusion"[12] or "massive transfer"[15,16] reactions) as "central" collisions. The location of this maximum shifts with fission detector geometry in exactly the manner predicted by the computer simulation (see Fig. 3). The location of the maximum corresponds to a transfer of ~92% of the beam momentum to the fissioning system.

The other component in the folding angle distribution peaks in the region of $\theta_{AB} \simeq 173°$. It is attributed to "peripheral" collisions such as inelastic scattering, breakup and transfer reactions. In a previous study[17,36], this component was observed in coincidence with projectile residues (Li, ..., O) detected close to the grazing angle. The minimum in the folding-angle distribution is a consequence of the fact that, for peripheral reactions, the largest cross sections are observed[36,40] for nitrogen and carbon fragments. For the very asymmetric detector

arrangement this minimum is less pronounced, mainly due to pile-up in the forward fission detector, which was subjected to high count rates.

2. Folding-Angle Distribution in Coincidence with Light Particles

The fission fragment folding-angle distributions measured in coincidence with p, d, t and α-particles are shown in Figs. 5 - 8. For reference, the inclusive distributions for geometries I and II are shown at the top of each figure. The folding-angle distributions observed in coincidence with light particles are shown below. They are labelled by the detection angle of the coincident light particle.

When light particles are observed at forward angles, the coincident fission fragment folding-angle distribution exhibits both "central" and "peripheral" components. This indicates that light particles are produced not only in "massive transfer" or "incomplete fusion" reactions, but also in "peripheral" reactions where a major portion of the beam momentum is carried off by projectile-like fragments. Protons, deuterons, and tritons are produced predominantly in "central" collisions whereas alpha particles have about equal contributions from both "central" and "peripheral" reactions. The large alpha-particle cross sections observed for "peripheral" collisions at forward angles may be explained as due to significant contributions from α-particle breakup of the ^{16}O projectile[9]. As the detection angle is increased, the relative contribution from small momentum transfer processes decreases to the point of being insignificant beyond about 50°.

If we assume that the unobserved particles are emitted isotropically (as is the case for thermal emission at low angular momenta), then the average recoil momentum can be calculated as the difference between the beam momentum and the average momentum of the observed light particle. The relationship between recoil momentum and folding angle (see Fig. 3) can then be used to determine the average folding angle which would be expected in this case. These average folding angles are marked by arrows in Fig. 5 - 8. They coincide with the corresponding peak locations of the large momentum transfer component. Therefore this component must be associated with a low multiplicity of precompound light particles. Since this component dominates the light-particle distributions at all angles, the emission of light particles is dominated by processes in which the target residue absorbs the major part of the beam momentum. This is in accordance with the pictures implied by the terms "incomplete fusion" or "massive transfer".

B. Light-Particle Angular Distributions

The folding angle between the two fission fragments can be used to classify "central" and "peripheral" collisions and study the corresponding light-particle spectra. For this purpose a cut corresponding to $P_R^{\parallel}/P_1 \approx 50\%$ has been introduced in the inclusive folding-angle distributions. Those events with larger recoil momenta were defined as "central" collisions and events with smaller recoil momenta as "peripheral" collisions. For the different detector geometries of this experiment this cut on θ_{AB} was adjusted to keep the ratio of "central" to "peripheral"

components in the inclusive distributions constant. The light-particle angular distributions, gated on "central" and "peripheral" collisions are shown in Fig. 9. The contribution from "central" collisions dominates the light-particle coincidence cross sections at all angles with the exception of the forward angle α-particle emission. (It should be kept in mind that our experimental arrangement might put a certain bias on the detection of central collisions as compared to peripheral collisions, see Section II.C.) Comparable alpha-particle cross sections are observed for "peripheral" and "central" processes. For "central" collisions the cross sections for the emission of deuterons and tritons are comparable in magnitude to the ones for proton and alpha-particle emission. In contrast, for compound nucleus evaporation, deuteron and triton emission is generally considered to be of minor importance[41]. The angular distributions for light particles produced in "peripheral" collisions exhibit a significantly steeper fall-off toward large angles than the corresponding cross sections for "central" collisions.

The multiplicity of light particles per fission event can be estimated by assuming the light-particle angular correlations to be symmetric about the beam axis. Rather low multiplicities of $M(p) = 0.39$, $M(d) = 0.18$, $M(t) = 0.15$ and $M(\alpha) = 0.44$ are obtained consistent with the qualitative conclusions reached by consideration of the momentum balance (see previous section). The multiplicities of hydrogen isotopes that are observed in "peripheral" reactions are lower by about a factor of two than the ones observed in "central"

reactions. (The multiplicity for a given gate on the folding angle is defined by the ratio of the integrated light particle yield and the inclusive fission yield observed for this gate. This procedure should, therefore, largely correct for the uncertainties in detection efficiencies that arise due to the unknown transverse momentum transfer distribution, see section II.C). For our particular choice of gates we obtain: $M_p(p) = 0.21$, $M_c(p) = 0.47$; $M_p(d) = 0.09$, $M_c(d) = 0.21$; $M_p(t) = 0.10$, $M_c(t) = 0.16$, where the subscripts p and c denote "peripheral" and "central" events. This observation might be explained by the fact that the "peripheral" gate includes inelastic scattering and rearrangement reactions that do not involve pre-equilibrium emission of light particles. The alpha-particle multiplicity of "peripheral" reactions, on the other hand, is larger than the one of "central" reactions: $M_p(\alpha) = 0.67$ vs. $M_c(\alpha) = 0.33$. This again indicates the importance of breakup reactions or sequential alpha-particle decay of the projectile residue for "peripheral" reactions induced by ^{16}O ions.

C. Light-Particle Energy Spectra

The energy spectra of protons produced in "central" collisions are qualitatively similar to the spectra of protons emitted in "peripheral" reactions, as is demonstrated in Fig. 10. Corresponding observations are made for the energy spectra of deuterons, tritons and alpha particles. This qualitative similarity of light-particle spectra in the two types of collisions indicates that the light particles are produced at an early stage of the reaction before the final fate of the projectile has been determined.

Since we find that the "central" contribution typically dominates the light-particle energy spectra and since there are no characteristics unique to either component of the light-particle energy spectra, we shall henceforth make no distinction between the two components and simply sum their contributions. These energy spectra are displayed in Figs. 11 - 14. At all angles the slopes of the energy spectra are inconsistent with evaporation from the compound nucleus. At forward angles, protons are emitted with energies of up to four times the beam energy per nucleon. With increasing detection angle, the light-particle cross sections decrease and the slopes of the energy spectra become steeper. Furthermore, at a given observation angle all light particles have energy spectra with similar slopes. In the context of a thermal model the slope can be associated with a temperature. This association implies that at a given angle all light particles are emitted with comparable temperatures and that these temperatures decrease as the detection angle increases.

The energy spectra of protons observed in this experiment are qualitatively similar to the inclusive energy spectra observed[23] for the similar reaction ^{197}Au (^{16}O, p) at 315 MeV. This corroborates our assumption that the fission coincidence requirement has placed little bias on the observed spectral shapes.

IV. DESCRIPTION OF ENERGY SPECTRA

A. Rotating Hot Spot Model

It has been proposed[8,14,20] that light-particle energy spectra having exponential slopes which are angle dependent may be understood in terms of emission from a nuclear "hot spot" which cools as it rotates. In this model, large frictional forces rapidly convert the relative motion of target and projectile into the excitation of internal degrees of freedom. This causes local heating in the region of contact. Simultaneously, part of the tangential motion of the system is transformed into collective rotational energy. Particle emission is assumed to occur from the heated region in the average direction of the tangential velocity at the surface. Because the emission angle can be related to the rotation time, the nuclear temperature deduced from the energy spectra will show an increasing degree of energy relaxation as the scattering angle is increased.

Particle evaporation in the frame of the composite system is assumed to occur from the hot spot following the statistical formula of Ericson[42]

$$N(E) \propto E\, \sigma_{inv}\, (E)\, \exp\, (-E/T) \qquad (2)$$

where E is the kinetic energy of the evaporated particle, σ_{inv} the inverse cross section, and T the nuclear temperature. Since the major energy dependence of σ_{inv} is a cutoff at the Coulomb barrier, we have simply included the effect of Coulomb repulsion from the target residue and treated σ_{inv} as a normalization

constant. After transforming to the laboratory frame and including the effects of the Coulomb barrier, we obtain

$$\frac{d^2N}{d\Omega dE} = N_o E'^{\frac{1}{2}}(E' - 2E'^{\frac{1}{2}}E_1^{\frac{1}{2}}\cos\theta + E_1)^{\frac{1}{2}}$$
$$\times \exp[-(E' - 2E'^{\frac{1}{2}}E_1^{\frac{1}{2}}\cos\theta + E_1)/T_\theta] \qquad (3)$$

Where N_o is a normalization constant for each spectrum, $E' = E - ZE_c$ is the energy before acceleration in the Coulomb field, E_c the Coulomb energy per unit charge, Z the charge of the emitted particle, T_θ the angle-dependent nuclear temperature and $E_1 = Mv^2/2$ is the kinetic energy of the particle of mass m at rest in the center of mass frame moving at velocity v.

Using eq. (3) with the compound nucleus velocity $v = .013c$ and with $E_c = 10$ MeV, it is possible to obtain quite satisfactory fits to the data (Figs. 11 - 14). At forward angles the agreement is somewhat worse, possibly due to contributions from non-thermal processes which are not included in this picture. The normalizations and temperatures used for the calculations of Figs. 11 - 14 are displayed in Table I. Except at forward angles, there is little variation of normalization with angle (in Ref. 14 the normalization was assumed to be constant with angle). The angle dependent temperatures T_θ extracted from the fits are shown in Fig. 15.

As a simple illustration of how such a model might be extended, we assume that the "hot spot" is at a uniform temperature and cools predominantly by convection with the surrounding nuclear matter. Classically, according to Newton's Law of Cooling, the

rate of heat loss, dQ/dt, is proportional to the temperature difference, $\Delta T = T - T_o$, between the hot region and its surroundings[43]

$$\frac{dQ}{dt} \propto \Delta T. \tag{4}$$

Ignoring the time and temperature dependence of the proportionality constant, we find that after a time, Δt, the temperature difference, ΔT, is related to the initial temperature difference, ΔT_i, by

$$\Delta T = \Delta T_i \exp(-\Delta t/\tau) \tag{5}$$

where τ is the characteristic decay time. The relaxation time, τ_R, is related to the decay time by integrating eq. (4)[43,44]

$$Q = \int_0^{\tau_R} dQ(t) = Q_o[1 - \exp(-\tau_R/\tau)] \tag{6}$$

Thus for practical purposes the relaxation time is a few times the decay time.

Classically, the decay time is given by[43] $\tau = \rho c R^2/\kappa N_{Nu}$ where ρ is the density, c the heat capacity, κ the thermal conductivity, R a characteristic length, and N_{Nu} a dimensionless number known as Nusselt's number. Substituting the thermal conductivity of nuclear matter[44], $\kappa \sim \rho c v_F \lambda$, where v_F is the Fermi velocity and λ the nucleon mean free path, we obtain[45]

$$\tau_R \sim \frac{R^2}{v_F \lambda} \tag{7}$$

in agreement with Ref. 44.

Substituting $\omega = \Delta\theta/\Delta t$ into eq. (5) we find

$$\Delta T = \Delta T_i \exp[-\Delta\theta/(\omega\tau)] \tag{8}$$

which is in accord with the experimentally observed decrease in temperature with angle (Fig. 15). If the hot region is assumed to cool toward the compound nucleus as the rest of the nucleus warms, then T_o should be taken as the compound nucleus temperature, $T_o = T_{cn} \simeq 3$ MeV. In Fig. 16 it is shown that if one considers only the region where the relative contribution from peripheral processes is insignificant (i.e. beyond about 30°), the quantity $\ln(T_\theta - T_o)$ is linearly related to θ for all light particles. Moreover, for deuterons, tritons and alpha particles the slope and intercept are very similar. For protons a flatter slope and smaller intercept are obtained which might be due to a larger compound nucleus contribution. The observed slope corresponds to $\omega\tau = 45.5$ degrees. Assuming a rotational velocity corresponding to a grazing collision with the moment of inertia of two touching spheres, we obtain a decay time of the order of $\tau = 3 \times 10^{-22}$ sec. This is about an order of magnitude shorter than observed at a lower incident energy[8]. The corresponding relaxation time of the "hot spot" is then of the order $\tau_R \simeq 10^{-21}$ sec which is in rough agreement with Ref. 46.

The rotating hot spot model fits the experimental data quite well and offers a physical explanation for several features of the data. However, in order to explain the experimental fact that the greatest temperatures are observed in the forward direction it was necessary to assume that the light particles are emitted tangentially from the hot spot. The physical justification for such an assumption is not clear. If the target and projectile are

assumed to stick together as they rotate, then due to absorption in the perpendicular directions the light particles should be emitted primarily in the tangential plane between the two nuclei. In this picture, the light-particle energy spectra should display an angle-dependent temperature which is symmetric about 90°. Instead, the observed light-particle energy spectra display temperatures which decrease continuously beyond 90°. Alternatively, the tangential emission might be a result of the rotational motion of the hot spot. However, in the present experiment the rotational energy at the nuclear surface is not expected to exceed about one MeV per nucleon and therefore will not dominate the thermal emission. (If very high rotational velocities of the hot spot could occur, eq. (3) would have to be modified to take the effect of rotation into account explicitly. Similar to Ref. 14 we have ignored this rotational velocity of the source with the result that the local nuclear temperature might be somewhat overestimated.)

B. Isotropic Emission from a Moving Source

Some qualitative insight on the overall trends of the data may be obtained by presenting the Lorentz invariant cross sections as a contour plot in the velocity plane. By means of such a diagram one can easily determine whether or not a rest frame exists from which the emission appears isotropic. If such a frame existed, the contours of constant cross section would appear as circles centered on the velocity of that frame. For emission from the compound nucleus these circular contours would be centered on the compound nucleus velocity, $v_{cn} = 0.013$ c. For emission from the

projectile the countours would be centered on the beam velocity $v_B = 0.205c$. A contour diagram of the Lorentz invariant proton cross sections is shown in Fig. 17. Levels of constant invariant cross section are indicated by the solid and open points. The points of equal cross section fall approximately on circles which are slightly flattened in the 90° region and are centered on a velocity of slightly less than half of the beam velocity.

We first investigate the question of whether it is possible that the protons are emitted from both the projectile and the compound nucleus giving a sum distribution which has the appearance of nearly isotropic emission from a single source at an intermediate velocity. In Fig. 18 we present contours of the Lorentz invariant proton cross sections gated on "central" or "peripheral" collisions. One might expect that such a gate should separate the compound nucleus contribution ("central" component) and the projectile contribution ("peripheral" component). It is evident from the figure that the gated contours do not follow these expectations, although the weaker peripheral component does exhibit a slight enhancement of emission from the projectile. The dominant feature of the Lorentz invariant contours, however, indicates nearly isotropic emission from a source which moves at slightly less than half of the beam velocity.

To be more precise, we assume that light particles are emitted with a Maxwellian distribution in the rest frame of a source[23] which is at temperature T.

$$N(E) \propto E^{\frac{1}{2}} \exp(-E/T). \qquad (9)$$

(Note that we use the $E^{\frac{1}{2}}$ factor corresponding to volume emission[47] instead of the factor E corresponding to surface emission. The difference between the two expressions would hardly be discernible except at low energies.) Transforming into the laboratory and correcting for the Coulomb repulsion of the light particle from the target residue, we obtain

$$\frac{d^2N}{d\Omega dE} = N_o f(v,T,E_c) = N_o(E - ZE_c)^{\frac{1}{2}}$$

$$x \exp\{-[(E - ZE_c) + E_1 - 2E_1^{\frac{1}{2}}(E - ZE_c)^{\frac{1}{2}}\cos\theta]/T\} \qquad (10)$$

where $E_1 = \frac{1}{2}Mv^2$ is the kinetic energy of a particle at rest in the frame of the moving source, N_o is an overall normalization constant and ZE_c is the Coulomb energy of the light particle with charge Z.

The curves in Fig. 17a represent contours which were produced assuming contributions from two sources

$$\frac{d^2N}{d\Omega dE} = N_{cn} f(v_{cn},T_{cn},E_{c,cn}) + N_p f(v_p,T_p,E_{c,p}) \qquad (11)$$

One source was assumed to correspond to emission from the compound nucleus; the corresponding parameters are $v_{cn} = 0.013c$ and $E_{c,cn} = 10$ MeV. The other source was assumed to correspond to emission from the fully accelerated projectile fragments which were assumed to move with the projectile velocity, $v_p = 0.205c$, and have negligible Coulomb barrier, $E_{c,p} = 0$. At the most backward angles, $\theta = 140°$, emission from the projectile is negligible and the parameters for emission from the compound nucleus can be determined rather unambiguously as $T_{cn} = 4.58$ MeV and $N_{cn} = 319$. Correspondingly, emission from the compound nucleus gives only minor contributions

to the most forward angles. Here the parameters for projectile emission can be determined rather unambiguously as $T_p = 3.85$ MeV and $N_p = 309$. The resulting energy and angle integrated relative contribution from the projectile-like source was found to be 75% of the compound nucleus source contribution. The calculation reproduces the data very well at forward and backward angles but significantly underestimates the cross section in the 90° region. Furthermore, the overall shapes of the contour lines that are predicted by this calculation are not observed experimentally.

A better description of the experimental data may be obtained by assuming isotropic emission in a rest frame that moves with a velocity intermediate between projectile and target. The temperature of such a source, as well as its velocity, are treated as free parameters to give an optimum description of the data. The results of such a calculation, obtained with eq. (1), are shown in Fig. 17b (and, for comparison, also in Figs. 18a and 18b). The Coulomb energy was fixed at $E_c = 10$ MeV and the source which best reproduced the proton energy spectra at all angles was determined to have a temperature of $T = 7.0$ MeV and a velocity which was slightly less than half of the beam velocity ($v = 0.091c$). The single source calculation gives satisfactory fits for large transverse momenta but becomes slightly worse in the forward and backward directions. The overall agreement is seen to be surprisingly good.

To make the discussion more quantitative, we compare these calculations with the measured energy spectra. In Fig. 19 the

proton energy spectra are shown with the cross sections calculated using eq. (11) for two moving sources. The solid curves were obtained with the same parameters as were used for the calculated contours of Fig. 17a. The dashed curves correspond to emission from the projectile at the distance of closest approach to the target. The projectile-like source was assumed to move with the velocity, $v_p = 0.18c$, corresponding to the velocity of the ^{16}O nuclei after deceleration in the Coulomb field of the target nucleus. A Coulomb barrier of $E_{c,p} = 10$ MeV was chosen and a temperature of $T = 3.94$ MeV was obtained by fitting the proton data at 15°. In this case the integrated contribution from the projectile-like source was only 59% of the compound nucleus source contribution. With either calculation the agreement with the data is quite good at both forward and backward angles but disagrees by as much as an order of magnitude in the intermediate angle region.

In Fig. 20 the solid curves have been calculated using eq. (10) with the same parameters as for the calculated contours of Fig.17b. The overall agreement with the proton data is seen to be remarkably good assuming only a single moving source. The agreement is certainly no worse than for the two source calculation.

Obviously, better reproduction of the data could be obtained by using two sources in which both source velocities were allowed to vary. At this point such a procedure would lead to complications and uncertainties of interpretation. Therefore, we proceed using the single source model and try to assess the significance

of the resulting parameters.

In Figs. 20 - 23 the curves were calculated using eq. (10) with a single moving source. The solid curves were obtained using a Coulomb repulsion per unit charge which had been chosen as $E_c = 10$ MeV. The dashed curves have been calculated by neglecting the Coulomb repulsion from the target residue. Clearly, the description of the data in the low energy region is better when the Coulomb effects are taken into account.

Some disagreement between calculation and the data is observed at forward angles. Here contributions from peripheral reactions are more important, especially for the case of alpha particles. We also find some discrepancy at backward angles where compound nucleus contributions are expected to be significant. We observe, however, that the overall trends of the data are reproduced remarkably well.

The thermal sources which best describe the light-particle spectra were found to have very similar velocities and temperatures. The rest frames in which the light particle emission appears isotropic were found to have velocities of $v/c = 0.091$, 0.096, 0.084, and 0.097 for p, d, t, and α-particles, respectively. It is interesting that these velocities closely coincide with the velocity , $v = 0.089c$, of the nucleon-nucleon center of mass frame if the slowing down of the ^{16}O nuclei in the Coulomb field of the ^{238}U target nuclei is taken into account. The source temperatures were found to be $T = 7.0$, 8.1, 8.8 and 7.7 MeV for p, d, t and α-particles, respectively. These temperatures are significantly larger than the temperature $T_{cn} \simeq 3$ MeV expected for the compound nucleus. If, instead one assumes the formation of a hot Fermi

gas consisting of an equal number of target and projectile nucleons, then significantly larger temperatures can be reached. For an ideal Fermi gas, the internal energy per nucleon, U/N, is given to lowest order in T by the relation[48]

$$U/N = 3/5\ \varepsilon_F \left[1 + \frac{5\pi^2}{12}\left(\frac{T_N}{\varepsilon_F}\right)^2\right] \qquad (12)$$

where ε_F is the Fermi energy. For a system of N nucleons consisting of equal contributions from target and projectile nuclei, $N_t = N_p = N/2$, the internal energy per nucleon for the system can alternatively be written as

$$U/N = 3/5\ \varepsilon_F + E^*/N = 3/5\ \varepsilon_F + 1/2\ m_o v_N^2 \qquad (13)$$

where E^* is the excitation energy of the N nucleons, m_o is the nucleon mass, and $2v_N$ is the relative velocity between target and projectile at the point of contact. From eqs. (12) and (13) the temperature of such a system is given by

$$T_N = (2m_o v_N^2 \varepsilon_F/\pi^2)^{\frac{1}{2}}, \qquad (14)$$

Using $v_N = 0.089c$ and the value of $\varepsilon_F = 38$ MeV corresponding to nuclear matter at normal density one obtains the value of $T_N = 7.5$ MeV in reasonable agreement with the experimentally determined values. However, it must be remembered that the dominant reaction process involves the transfer of nearly the entire beam momentum to the target residue (see sect. III. A and B). As a consequence any such hot gas of nucleons must ultimately be absorbed by the target

nucleus. Furthermore, the similarity of the light-particle energy spectra for large and small momentum transfers implies that particle emission occurs on a time scale which is comparable to the time scale for energy and momentum transfer from the hot gas to the target nucleus. Our data are therefore consistent with prompt emission from a "hot spot" for which the thermalization of the nucleon velocities occurs first in the nucleon-nucleon center of mass frame. In fact, the prompt proton emission might occur after only a single nucleon-nucleon collision; in this event the apparent thermalization of the nucleon velocities would be a result of the intrinsic Fermi motion[49,50].

V. PRODUCTION OF COMPOSITE PARTICLES

A. Coalescence Model

As was pointed out in the previous section, very similar slopes are observed for the energy spectra of different light particles. In the context of the thermal model discussed in the previous section this implied particle emission from a source of rather well defined temperature. As a consequence one expects the validity of a simple power law relating composite particle spectra to the proton spectra according to

$$e^{-E/T} \sim (e^{-E/AT})^A. \qquad (15)$$

Similar observations[51-53] have been made for light particles emitted in relativistic heavy ion collisions, i.e. the emission of composite particles has been related to proton emission via a coalescence model[51-58]. The complex particles are assumed to be synthesized by the coalescence of free nucleons which happen to occupy the same region of momentum space[55]. Since this prescription has had great success at relativistic energies, it is interesting to investigate the validity of the model at non-relativistic energies. However, at lower energies the influence of the Coulomb field of the target residue cannot be neglected as has been done at relativistic energies (see also Sect. IV. B). If the effect of the Coulomb repulsion of the charged particles from the target residue is taken into account one obtains a generalized coalescence relation

$$\frac{d^2N(Z,N,E_A)}{dE_A d\Omega} = \left(\frac{N_t + N_p}{Z_t + Z_p}\right)^N \frac{A^{-1}}{N!Z!} \left[\frac{\frac{4\pi}{3} P_0^3}{\{2m^3(E-E_c)\}^{\frac{1}{2}}}\right]^{A-1} \left(\frac{d^2N(1,0,E)}{dEd\Omega}\right)^A \qquad (16)$$

The derivation of this relation is given in Appendices A and B. It is different from the relation quoted in Ref. 24. In eq. (16) E_c is the Coulomb repulsion per unit charge, $d^2N(Z,N,E_A)/dE_A d\Omega$ is the differential multiplicity of nuclei composed of Z protons and $N = A - Z$ neutrons, and $E_A = AE - NE_c$. The coalescence radius in momentum space, P_o, is the only free parameter.

The differential multiplicity for a given event is not a measured quantity. In practice, it is approximated by the average differential multiplicity[51,53]. For the present analysis we use the corresponding approximation

$$\frac{d^2N(Z,N)}{dE_A d\Omega} = \frac{1}{N_f} \frac{d^2N_f(Z,N)}{dE_A d\Omega}, \qquad (17)$$

where $N_f(Z,N)$ is the number of light particles observed in coincidence with fission and N_f is the total number of fission events.

In Fig. 24 the energy spectra of deuterons (solid points) are compared with the predictions of the coalescence model which has not been modified to take Coulomb effects into account (dashed lines). Without the Coulomb modifications the coalescence model is unable to relate the composite particle cross sections to the proton cross sections.

In Figs. 24 - 26 the energy spectra of deuterons, tritons and alphas (solid points) are compared with the predictions of the Coulomb-modified coalescence relation (open squares). For deuterons and tritons the agreement with the data is excellent except at the most backward angles. Here a discrepancy might be anticipated because contributions from compound nucleus evaporation are expected

to be non-negligible for protons but of minor importance for the case of deuterons and tritons[41]. Consequently, the coalescence calculations will overestimate the cross sections at backward angles, in accordance with Figs. 24 and 25. For the alpha-particle spectra (Fig. 26) the coalescence predictions are also in fair agreement with the data. Here larger discrepancies are expected to occur also at forward angles, because of the enhanced contributions from projectile breakup reactions, due to the alpha-cluster structure of the ^{16}O projectile.

To be consistent with our previous analysis, the Coulomb energy per unit charge E_c has been kept fixed at the value $E_c = 10$ MeV. The coalescence radii of $P_o(d) = 170$ MeV/c, $P_o(t) = 215$ MeV/c, and $P_o(\alpha) = 270$ MeV/c were used for the calculations of the deuteron, triton, and alpha-particle spectra respectively. These radii are very similar to typical values measured for relativistic heavy ion collisions[53]. (Some differences are to be expected due to the different normalizations of the differential multiplicities used at relativistic energies and for the present experiment --see the discussion of eqs. (17) and (A10)). At relativistic energies, P_o has been observed to be essentially independent of incident energy[53]. It is remarkable that the coalescence radius should show so little dependence on the incoming energy over such a wide range of incident energies.

Several physical models have been proposed[51-58] which relate the composite-particle spectra to the proton spectra in the same manner as the coalescence relation. Each of these models predicts

a different form for the radius parameter, P_o, using assumptions on the production mechanism which range from a nonequilibrium final state interaction[54] to thermodynamic equilibrium[56]. In several of these models the coalescence radius is expected to depend on the incident energy. For example, in the classical limit of the thermodynamic model a temperature dependence of $P_o \sim kT$ is predicted. Therefore, the observed independence of P_o on the incident energy is in contrast to the expectations of such models.

If the thermodynamic interpretation[56] of the coalescence model applies, the momentum radius P_o can be related to the volume of the thermal system at the freeze-out density where formation and breakup of composite particles ceases[53,56]

$$V = \left(\frac{Z!N!A^3}{2^A} (2s+1) \exp(E_o/T) \right)^{1/(A-1)} \frac{3h^3}{4\pi P_o^3} , \qquad (18)$$

where E_o is the binding energy and s is the spin of the composite particle. Freeze-out radii of $R(d) = 5.6$ fm, $R(t) = 4.2$ fm, and $R(\alpha) = 3.7$ fm result from eq. (18). Such radii appear consistent with emission from a locally heated region of the nucleus.

We conclude that the coalescence relation can be successfully applied at nonrelativistic as well as relativistic energies. This observation makes possible a coherent study of light-particle emission over a broad range of incident energies. Such a study may ultimately provide a test ground for the various models that have been used to derive the coalescence relation formally.

B. Entropy

It has been suggested[59] that the relative production of protons and deuterons may be used to calculate the entropy which is produced in the early stages of the nuclear collision. After the initial stage of the reaction, the fireball is assumed to expand through chemical equilibrium until it reaches the composite-particle freeze-out density (this is the assumption underlying the thermodynamic model of Ref. 56). If the system of nucleons can be described in terms of an ideal gas and if one assumes that neutrons and protons have identical chemical potentials, then the usual relations for the entropy and chemical equilibrium of an ideal gas give the entropy per nucleon to be[59,60]

$$S/N(A:p) = 5/2 + \frac{1}{(A-1)}\left[\varepsilon_A/T + \ln\left(\frac{g_A}{g_p}\left(\frac{m_A}{m_p}\right)^{3/2}\right) - \ln R_{Ap}\right] \qquad (19)$$

where R_{Ap} is the ratio of composite particles of A nucleons to protons, g is the spin degeneracy, and ε_A is the binding energy of the composite particle. If the expansion of the fireball is further assumed to be nearly adiabatic, this entropy then corresponds to the entropy produced in the early stages of the reaction.

With the observed proton and deuteron multiplicities, M(p) = 0.39 and M(d) = 0.18 (see sect. II. B), an entropy per nucleon of S/N = 5.0 is calculated. This value appears to follow the same trend as the experimental entropies deduced at relativistic energies. The entropy calculated by assuming a soft equation of state for nuclear matter is considerably less than the experimental values[59]. An attempt to amend this discrepancy was made by

postulating[59] that unknown degrees of freedom in nuclear matter such as collective effects or nucleon dissociation were being excited.

Unless further assumptions are made, the entropy per nucleon should not depend on which light particle ratio is used in eq. (19). With our observed triton and alpha particle multiplicities, M(t) = 0.15 and M(α) = 0.44, one obtains S/N(t:p) = 4.3 and S/N(α:p) =4.1. If the various emitted particles carry information of a common state of entropy, then these discrepancies in the calculated entropy imply (note the weak logarithmic dependence on particle ratio), that the observed particle ratios deviate significantly from the particle ratios which would be expected for an ideal gas in chemical equilibrium.

In order to justify a treatment in terms of an ideal gas, the density of the system of nucleons must be much less than the so-called critical density n_c[48]

$$n << n_c = g\left(\frac{mT}{2\pi\hbar^2}\right)^{3/2}, \qquad (20)$$

where m is the nucleon mass, T the temperature of the system, and g is the nucleon degeneracy factor. In the present analysis, with T = 10 MeV we must have $n << 0.09 n_o$ where $n_o = 0.17$ fm^{-3} is the normal nuclear density. This condition is unlikely to be satisfied. Even at relativistic energies where T = 80 MeV the strong condition $n << 2n_o$ might not be very well fulfilled. As a consequence, thermodynamic treatments which use the ideal gas formalism such as the present model[59] and the thermodynamic interpretation of the

coalescence model[56] should be treated with care at relativistic energies and, probably, should not be applied in the nonrelativistic regime.

VI. SUMMARY AND CONCLUSION

We have studied light particles emitted in ^{16}O-induced reactions on ^{238}U at 20 MeV/nucleon beam energy in coincidence with the fission decay of the target residue. The measured folding angle between two coincident fission fragments was used to provide information on the linear momentum transferred to the target residue prior to fission. This information has been used for a simple operational classification of the reaction into "central" and "peripheral" collisions corresponding to large and small momentum transfers to the target residue.

The majority of energetic light particles has been shown to be associated with "central" collisions in which nearly the entire beam momentum is transferred to the target residue. Consistent with this observation are average p, d, t and α-particle multiplicities of less than one.

Light particles emitted in "peripheral" reactions have displayed angular distributions which are more strongly forward peaked than those of "central" collisions. On the other hand, the energy spectra have been shown to be rather similar for the two processes. This similarity of energy spectra suggests a reaction mechanism in which the light particles are emitted at an early stage of the reaction.

The emission of light particles is approximately isotropic in a rest frame moving with about half of the beam velocity. In this frame the energy spectra can be described by thermal emission at the temperature of a Fermi gas consisting of an equal number of nucleons from target and projectile. This

observation could be an indication of the importance of knock-out processes in which the apparent thermalization would be a result of simple Fermi motion. Although such a mechanism might explain proton emission,[49] it is not yet clear how the emission of composite particles fits into such a picture. We have shown, however, that the composite-particle spectra may be understood in terms of the proton spectra via a coalescence relation which has been modified to include the effects of Coulomb distortion. This allows composite-particle emission to be treated systematically within a single framework throughout the relativistic and nonrelativistic realms of heavy-ion reactions. It will be interesting to make such a systematic study of the incident energy dependence of the coalescence radius in order to determine the correct physical interpretation of the coalescence relation.

VII. ACKNOWLEDGEMENTS

We wish to extend our appreciation to Professor G. Bertsch for his interest and for many illuminating discussions about the interpretation of the present experimental results. The 88"-cyclotron operating staff did an outstanding job of providing the difficult $^{16}O^{6+}$ beams for the present study. The metallic ^{238}U targets produced by C. Ellsworth were greatly appreciated. We wish to acknowledge the assistance of Dr. T.J.M. Symons during the experiment and of R. Ellis in preparing many of the figures for this publication. This work is supported in part by the National Science Foundation under grant No. PHY 78-22696 and in part by the Office of Basic Energy Sciences, Division of Nuclear Sciences, U.S. Department of Energy.

APPENDIX A: COALESCENCE MODEL FOR POISSON MULTIPLICITY DISTRIBUTION

The basic assumption of the coalescence model is that complex particles are formed by the coalescence of nucleons which happen to share the same volume element of momentum space[55]. The critical radius, P_o, within which coalescence occurs is treated as a free parameter. The probability, P, for finding one primary nucleon in the coalescence volume centered at a momentum per nucleon, $\vec{p}$, is given by the product of this volume with the single nucleon momentum density

$$P = \frac{4\pi}{3} P_o^3 \frac{1}{\bar{m}} \frac{d^3N(\vec{p})}{dp^3} , \tag{A1}$$

where $\frac{d^3N(\vec{p})}{dp^3}$ represents the differential nucleon multiplicity and $\bar{m}$ is the average nucleon multiplicity.

For a given multiplicity, m, i.e. when m nucleons are produced in an event, the probability of finding n of them ($n \leq m$) in the coalescence volume will be given by the binomial distribution

$$P(n|m) = \binom{m}{n} P^n (1-P)^{m-n} . \tag{A2}$$

In actuality, each multiplicity will have a probability f(m) of occurrence. Summing over this distribution of multiplicities, we obtain the average probability for finding n nucleons in the coalescence volume.

$$\langle P(n) \rangle = \sum_{m \geq n} f(m) P(n|m) = \sum_{m \geq n} f(m) \binom{m}{n} P^n (1-P)^{m-n} . \tag{A3}$$

In the case of low average multiplicities, $\bar{m}$, as in the present experiment, it is reasonable to assume a Poisson distribution of multiplicities

$$f(m) = \frac{(\bar{m})^m}{m!} e^{-\bar{m}} . \tag{A4}$$

Substituting eq. (A4) into eq. (A3), we obtain an average probability given by

$$\begin{aligned} \langle P(n) \rangle &= \sum_{m \geq n} \frac{(\bar{m})^m}{m!} e^{-\bar{m}} \frac{m!}{n!(m-n)!} P^n (1-P)^{m-n} \\ &= \frac{(\bar{m}P)^n e^{-\bar{m}}}{n!} \sum_{\nu \geq 0} \frac{1}{\nu!} ((1-P)\bar{m})^\nu \\ &= \frac{(\bar{m}P)^n e^{-\bar{m}P}}{n!} . \end{aligned} \tag{A5}$$

Eq. (A5) is exact for a Poisson multiplicity distribution. At relativistic energies large multiplicities are observed with a non-Poisson distribution[61]. In this case it is assumed that eq. (A3) can be approximated by

$$\langle P(n) \rangle \simeq P(n|\bar{m}) = \binom{\bar{m}}{n} P^n (1-P)^{\bar{m}-n} . \tag{A6}$$

Then if $P \ll 1$ and $\bar{m} \gg n$ the binomial distribution becomes Poisson in form which again results in eq. (A5).

Typically, the exponential term in eq. (A5) can be ignored since $\bar{m}P$ is small. This gives the average probability for having N neutrons and Z protons in the coalescence sphere to be

$$\langle P(N,Z) \rangle = \frac{(\bar{m}_Z P_Z)^Z}{Z!} \frac{(\bar{m}_N P_N)^N}{N!} , \tag{A7}$$

where we have assumed that the probabilities for the observation of neutrons and protons are independent. In the context of the coalescence model P(N,Z) represents the probability of forming a composite particle with momentum per nucleon $\vec{p}$.

Since the neutron distributions typically are not measured, we assume that they have the same shape as the proton distributions but are weighted by the N/Z ratio of the composite system

$$\frac{d^3N(0,1)}{dp^3} = \frac{N_t + N_p}{Z_t + Z_p} \frac{d^3N(1,0)}{dp^3} \quad . \tag{A8}$$

Substituting eqs. (A1) and (A8) into Eq. (A7) and dividing by the coalescence volume, we obtain the composite particle momentum distribution in the form of the usual coalescence relation[51-53,56,58] used at relativistic energies

$$\frac{d^3N(Z,N)}{dp^3} = \left(\frac{N_t + N_p}{Z_t + Z_p}\right)^N \frac{1}{N!Z!} \left(\frac{4\pi}{3} p_o^3\right)^{A-1} \left(\frac{d^3N(1,0)}{dp^3}\right)^A . \tag{A9}$$

It is important to note that the differential nucleon multiplicity per event, d^3N/dp^3, is chosen by normalizing the experimentally observed momentum distribution to the class of events of interest

$$\frac{d^3N}{dp^3} = \frac{1}{\sigma_o} \frac{d^3\sigma}{dp^3} \quad . \tag{A10}$$

At relativistic energies this class of events has been chosen to consist of all possible reactions[51-53]. Therefore, the total reaction cross section, σ_R, is substituted for σ_o. Due to the restriction of the fission coincidence requirement of this experiment, we have analogously chosen to normalize our momentum distributions to inclusive fission events (see eq. 17). It should be clear from eqs. (A9) and (A10) that this choice of normalization enters directly into the interpretation of P_o.

APPENDIX B: MODIFICATION OF COALESCENCE RELATION BY COULOMB FIELD

We calculate the modification to the coalescence relation of Appendix A (eq. A9) which results when the coalescence occurs in the vicinity of a stationary Coulomb source[62] such as at the nuclear surface. The energy balance for a particle of charge Z and mass number A can be written as

$$\frac{p_A^2}{2mA} = \frac{p_{A_o}^2}{2mA} + ZE_c \quad , \tag{B1}$$

where E_c is the Coulomb energy per unit charge of the composite particle, p_{A_o} is the momentum of the composite particle at the nuclear surface, and p_A is the momentum of the particle in the laboratory. Eq. (B1) can be rewritten as

$$p_{A_o} = p_A\left(1 - \frac{2mAZE_c}{p_A^2}\right)^{\frac{1}{2}} \quad . \tag{B2}$$

From eq. (B1) we see that

$$p_A dp_A = p_{A_o} dp_{A_o} \quad . \tag{B3}$$

By using eq. (B2) we obtain

$$p_{A_o}^2 dp_{A_o} = p_{A_0} p_A dp_A = \left(1 - \frac{2mAZE_c}{p_A^2}\right)^{\frac{1}{2}} p_A^2 dp_A \tag{B4}$$

Analogously for a proton we have $Z = A = 1$ which gives

$$p_o^2 dp_o = \left(1 - \frac{2mE_c}{p^2}\right)^{\frac{1}{2}} p^2 dp \quad . \tag{B5}$$

We then assume that

$$p_{A_o} = Ap_o \quad , \tag{B6}$$

and also that the Coulomb field does not change the angular directions

$$d\Omega_A = d\Omega_{A_o}, \quad d\Omega = d\Omega_o . \tag{B7}$$

The coalescence relation of eq. (A9) then states that at the nuclear surface the composite-particle cross section is related to the proton cross section according to

$$\frac{d^3N(Z,N)}{dp_o^3} = C\left(\frac{d^3N(1,0)}{dp_o^3}\right)^A , \tag{B8}$$

where

$$C = \left(\frac{N_t + N_p}{Z_t + Z_p}\right)^N \frac{1}{N!Z!}\left(\frac{4\pi}{3} p_o^3\right)^{A-1} . \tag{B9}$$

Transforming the light-particle cross sections into the laboratory frame by using eqs. (B4) (B5) and (B7), we obtain the Coulomb-modified coalescence relation in momentum space

$$\frac{d^2N(Z,N)}{p_A^2 dp_A d\Omega} = CA^{-3} \frac{(1 - 2mAZE_c/p_A^2)^{1/2}}{(1 - 2mE_c/p^2)^{A/2}} \left(\frac{d^2N(1,0)}{p^2 dp d\Omega}\right)^A . \tag{B10}$$

We now transform eq. (B10) into energy space by first rewriting it as

$$\frac{d^2N(Z,N)}{p_A dp_A d\Omega} = CA^{-3} \frac{(p_A^2 - 2mAZE_c)^{1/2}}{(p^2 - 2mE_c)^{A/2}} \left(\frac{d^2N(1,0)}{pdpd\Omega}\right)^A , \tag{B11}$$

and then using

$$p_A^2 = 2mAE_A, \quad p^2 = 2mE , \tag{B12}$$

and

$$p_A dp_A = mAdE_A, \quad pdp = mdE . \tag{B13}$$

This gives

$$\frac{d^2N(Z,N)}{mAdE_A d\Omega} = \frac{CA^{-3}}{(2m)^{(A-1)/2}} \frac{(AE_A - ZAE_c)^{1/2}}{(E-E_c)^{A/2}} \left(\frac{d^2N(1,0)}{mdEd\Omega}\right)^A , \tag{B14}$$

or

$$\frac{d^2N(Z,N)}{dE_A d\Omega} = \frac{CA^{-1}}{(2m^3)^{(A-1)/2}} \frac{((E_A - ZE_c)/A)^{1/2}}{(E - E_c)^{A/2}} \left(\frac{d^2N(1,0)}{dEd\Omega}\right)^A . \tag{B15}$$

Finally noting that

$$E_A - ZE_c = E_{A_o} = AE_o = A(E - E_c) , \tag{B16}$$

we obtain a coalescence relation which is valid when the coalescence occurs in the vicinity of a Coulomb field

$$\frac{d^2N(Z,N,E_A)}{dE_A d\Omega} = \left(\frac{N_t + N_p}{Z_t + Z_p}\right)^N \frac{A^{-1}}{N!Z!} \left[\frac{\frac{4\pi}{3} p_o^3}{(2m^3(E-E_c))^{1/2}}\right]^{A-1} \left(\frac{d^2N(1,0,E)}{dEd\Omega}\right)^A . \tag{B17}$$

References

1. J. Péter, M. Berlanger, C. Ngô, B. Tamain, B. Lucas, C. Mazur, M. Ribrag and C. Signarbieux, Z. Physik A283, 413 (1977).

2. Y. Eyal, A. Gavron, I. Tserruya, Z. Fraenkel, Y. Eisen, S. Wald, R. Bass, G.R. Gould, G. Kreyling, R. Renfordt, K. Stelzer, R. Zitzmann, A. Gobbi, U. Lynen, H. Stelzer, I. Rode and R. Bock, Phys. Rev. Lett. 41, 625 (1978).

3. D. Hilscher, J.R. Birkelund, A.D.Hoover, W.U. Schröder, W.W. Wilcke, J.R. Huizenga, A.C. Mignerey, K.L. Wolf, H.F. Breuer and V.E. Viola, Jr., Phys. Rev. C20, 576 (1979).

4. G.R. Gould, R. Bass, J.v. Czarnecki, V. Hartmann, K. Stelzer, R. Zitzmann and Y. Eyal, Z. Physik A294, 323 (1980).

5. H.C. Britt and A.R. Quinton, Phys. Rev. 124, 877 (1961).

6. J.B. Ball, C.B. Fulmer, M.L. Mallory, and R.L. Robinson, Phys. Rev. Lett 40, 1698 (1978).

7. J.W. Harris, T.M. Cormier, D.F. Geesaman, L.L. Lee, Jr., R.L. McGrath and J.P. Wurm, Phys. Rev. Lett. 38, 1460 (1977).

8. H.Ho, R. Albrecht, W. Dünnweber, G. Graw, S.G. Steadman, J.P. Wurm, D. Disdier, V. Rauch and F. Scheibling, Z. Physik A283, 235 (1977).

9. C.K. Gelbke, M. Bini, C. Olmer, D.L. Hendrie, J.L. Laville, J. Mahoney, M.C. Mermaz, D.K. Scott and H.H. Wieman, Phys. Lett. 71B, 83 (1977).

10. T. Inamura, M. Ishihara, T. Fukuda, T. Shimoda and H. Hiruta, Phys. Lett. 68B, 51 (1977).

11. T. Nomura, J. Delaunay, C. Tosello and N. Bendjaballah, Nucl. Phys. A305, 262 (1978).

12. L. Westerberg, D.G. Sarantites, D.C. Hensley, R.A. Dayras, M.L. Halbert and J.H. Barker, Phys. Rev. C18, 796 (1978).

13. R.K. Bhowmik, E.C. Pollacco, N.E. Sanderson, J.B.A. England and G.C. Morrison, Phys. Rev. Lett. 43, 619 (1979).

14. T. Nomura, H. Utsunomiya, T. Motobayashi, T. Inamura and M. Yanokura, Phys. Rev. Lett. 40, 694 (1978).

15. D.R. Zolnowski, H. Yamada, S.E. Cala, A.C. Kahler and T.T. Sugihara, Phys. Rev. Lett. 41, 92 (1978).

16. H. Yamada, D.R. Zolnowski, S.E. Cala, A.C.Kahler, J. Pierce and T.T. Sugihara, Phys. Rev. Lett. 43, 605 (1979).

References (continued)

17. T.C. Awes, C.K. Gelbke, B.B. Back, A.C. Mignerey, K.L. Wolf, P. Dyer, H. Breuer and V.E. Viola, Jr., Phys. Lett. 87B, 43 (1979).

18. K. Siwek-Wilczyńska, E.H. du Marchie van Voorthuysen, J. van Popta, R.H. Siemssen, and J. Wilczyński, Phys. Rev. Lett. 42, 1599 (1979) and Nucl. Phys. A330, 150 (1979).

19. T. Inamura, T. Kojima, T. Nomura, T. Sugitate and H. Utsunomiya, Phys. Lett. 84B, 71 (1979).

20. H. Utsunomiya, T. Nomura, T. Inamura, T. Sugitate and T. Motobayashi, Nucl. Phys. A334, 127 (1980).

21. J.R. Wu, and I.Y. Lee, Phys. Rev. Lett. 45, 8 (1980).

22. J.H. Barker, J.R. Beene, M.L. Halbert, D.C. Hensley, M. Jääskeläinen, D.G. Sarantites, and R. Woodward, Phys. Rev. Lett. 45, 424 (1980).

23. T.J.M. Symons, P. Doll, M. Bini, D.L. Hendrie, J. Mahoney, G. Mantzouranis, D.K. Scott, K. van Bibber, Y.P. Viyogi, H.H. Wieman and C.K. Gelbke, Phys. Lett. 94B, 131 (1980).

24. T.C. Awes, C.K. Gelbke, G. Poggi, B.B. Back, B. Glagola, H. Breuer, V.E. Viola, Jr., and T.J.M. Symons, Phys. Rev. Lett. 45, 513 (1980).

25. P.A. Gottschalk and M. Weström, Phys. Rev. Lett. 39, 1250 (1977) and Nucl. Phys. A314, 232 (1979).

26. S.I.A. Garpman, D. Sperber and M. Zielinska-Pfabe, Phys. Lett. 90B, 53 (1980).

27. S.I.A. Garpman, S.K. Samaddar, D. Sperber and M. Zielinska-Pfabe, Phys. Lett. 92B, 56 (1980).

28. C.K. Cline and M. Blann, Nucl. Phys. A172, 225 (1971).

29. G.D. Harp and J.M. Miller, Phys. Rev. C3, 1847 (1971).

30. M. Blann, Nucl. Phys. A235, 211 (1974).

31. H.W. Bertini, R.T. Santoro and O.W. Hermann, Phys. Rev. C14, 590 (1976).

32. J.P. Bondorf, J.N. De, A.O.T. Karvinen, G. Fái and B. Jakobsson, Phys. Lett. 84B, 162 (1979).

33. J.P. Bondorf, J.N. De, G. Fái, A.O.T. Karvinen, B. Jakobsson and J. Randrup, Nucl. Phys. A333, 285 (1980).

References (continued)

34. M. Blann, Phys. Lett. 88B, 5 (1979), and Phys. Rev. C21, 1770 (1980).

35. T. Sikkeland, E.L. Haines and V.E. Viola, Jr., Phys. Rev. 125, 1350 (1962).

36. B.B. Back, K.L. Wolf, A.C. Mignerey, C.K. Gelbke, T.C. Awes, H. Breuer, V.E. Viola, Jr., and P. Dyer, Phys. Rev. C22, 1927 (1980).

37. C. Maples, Program LZY, unpublished.

38. H.W. Schmitt, W.E. Kiker and C.W. Williams, Phys. Rev. 137, B837 (1965).

39. F.S. Goulding and B.G. Harvey, Ann. Rev. Nucl. Sci. 25, 167 (1975).

40. C.K. Gelbke, C. Olmer, M. Buenerd, D.L. Hendrie, J. Mahoney, M.C. Mermaz and D.K. Scott, Phys. Reports 42, 311 (1978).

41. F. Pühlhofer, Nucl. Phys. A280, 267 (1977).

42. T. Ericson, Adv. Phys. 9, 425 (1960).

43. See e.g. A.J. Chapman, in Heat Transfer (The Macmillan Co., 1967) ; or A.V. Luikov, in Analytical Heat Diffusion Theory (Academic Press, 1968)

44. R. Weiner and M. Weström, Nucl. Phys. A286, 282 (1977).

45. D.K. Scott, Lectures delivered at the NATO/NSF Advanced Studies Institute on Theoretical Methods in Medium-Energy and Heavy-Ion Physics, Madison, Wisconsin, June 12 - 23, 1978.

46. M. Blann, A. Mignerey, W. Scobel, Nukleonika 21, 335 (1976).

47. A.S. Goldhaber, Phys. Rev. C17, 2243 (1978).

48. R.K. Pathria, in Statistical Mechanics (Pergamon Press, 1972)

49. D. Cha and G. Bertsch, to be published.

50. J. Hüfner and M.C. Nemes, preprint.

51. H.H. Gutbrod, A. Sandoval, P.J. Johansen, A.M. Poskanzer, J. Gosset, W.G. Meyer, G.D. Westfall and R. Stock, Phys. Rev. Lett. 37, 667 (1976).

52. J. Gosset, H.H. Gutbrod, W.G. Meyer, A.M. Poskanzer, A. Sandoval, R. Stock and G.D. Westfall, Phys. Rev. C16, 629 (1977).

53. M.-C. Lemaire, S. Nagamiya, S. Schnetzer H. Steiner and I. Tanihata, Phys. Lett. 85B, 38 (1979).

54. S.T. Butler and C.A. Pearson, Phys. Rev. 129, 836 (1963).

55. A. Schwarzschild and Č. Zupančič, Phys. Rev. 129, 854 (1963).

56. A. Mekjian, Phys. Rev. Lett. 38, 640 (1977); Phys. Rev. C17, 1051 (1978); Phys. Lett. 89B, 177 (1980).

57. R. Bond, P.J. Johansen, S.E. Koonin and S. Garpman, Phys. Lett. 71B, 43 (1977).

58. J.I. Kapusta, Phys. Rev. C21, 1301 (1980).

59. P.J. Siemens and J.I. Kapusta, Phys. Rev. Lett. 43, 1486 (1979); and I.M. Mishustin, F. Myhrer and P.J. Siemens, preprint.

60. G. Bertsch, private communication.

61. A. Sandoval, H.H. Gutbrod, W.G. Meyer, R. Stock, Ch. Lukner, A.M. Poskanzer, J. Gosset, J.-C. Jourdain, C.H. King, G. King, Nguyen Van Sen, G.D. Westfall and K.L. Wolf, Phys. Rev. C21, 1321 (1980).

62. M. Gyulassy and S.K. Kauffmann, Lawrence Berkeley Laboratory Report, LBL 10279 (1980).

FIGURE CAPTIONS

Fig. 1. Experimental geometry used in present study.

Fig. 2. Fission fragment detection efficiency as a function of the fission fragment folding angle θ_{AB} obtained by simulation of the fission of ^{254}Fm with the two experimental geometries of the present experiment.

Fig. 3. Dependence of the average folding angle θ_{AB} on $P_R^{||}$ as calculated from the simulated fission of ^{238}U and ^{254}Fm nuclei moving parallel to the beam axis. The relationship is shown for the two experimental geometries. (P_1 is the beam momentum).

Fig. 4. Folding-angle distributions of fission fragments measured inclusively for the experimental geometries of this experiment ($\theta_A^o = -60°$, $\theta_B^o = 100°$ and $\theta_A^o = -75°$, $\theta_B^o = 85°$) and for a symmetric setting ($\theta_A^o = -\theta_B^o = -80°$).

Fig. 5. Folding-angle distributions of fission fragments measured inclusively and in coincidence with protons for the two experimental geometries of this experiment. The detection angles of the coincident protons are given in the figure. The arrows are described in section III.A.2.

Fig. 6. Folding-angle distributions of fission fragments measured inclusively and in coincidence with deuterons for the two experimental geometries of this experiment. The detection angles of the coincident deuterons are given in the figure. The arrows are described in section III.A.2.

TABLE I. Normalizations and temperatures used in "rotating hot spot" calculations of Figs. 11-14.

Angle	Normalization, N_o				Temperature, T_θ (MeV)			
	Protons	Deuterons	Tritons	Alphas	Protons	Deuterons	Tritons	Alphas
15°	124	40	28	1350	8.96	12.6	14.8	10.7
25	92	23	16	268	8.74	12.1	13.6	11.5
40	78	19	14	60	8.34	11.2	12.3	11.5
55	86	22	12	42	6.51	8.36	9.76	8.88
70	68	20	9.0	29	6.05	6.84	8.18	7.44
95	67	18	9.6	13	4.76	5.18	5.83	5.72
110	63	13	11	12	4.24	4.86	4.81	4.97
125	82	25	13	19	4.15	4.00	4.41	4.41
140	86	25	13	29	3.97	3.87	4.07	4.16

Fig. 7. Folding-angle distributions of fission fragments measured inclusively and in coincidence with tritons for the two experimental geometries of this experiment. The detection angles of the coincident tritons are given in the figure. The arrows are described in section III.A.2.

Fig. 8. Folding-angle distributions of fission fragments measured inclusively and in coincidence with alpha particles for the two experimental geometries of this experiment. The detection angles of the coincident alpha particles are given in the figure. The arrows are described in section III.A.2.

Fig. 9. Angular distributions of light particles, p, d, t and α, in coincidence with fission fragments produced in central and peripheral collisions. The sum of the two contributions is also shown. The lower energy cutoffs are given in the figure. The cross sections are normalized to fission singles.

Fig. 10. Energy spectra of protons detected in the reaction ^{238}U (^{16}O, pf) at 315 MeV gated by "central" and "peripheral" collisions. The spectra are labelled by the detection angle of the coincident protons. The cross sections are normalized to fission singles.

Fig. 11. Energy spectra of protons detected in the reaction ^{238}U (^{16}O, pf) at 315 MeV. The spectra are labelled by the detection angle of the coincident protons. The cross sections are normalized to fission singles. The data are fitted with the rotating hot spot model of eq. (3).

Fig. 12. Energy spectra of deuterons detected in the reaction ^{238}U (^{16}O, df) at 315 MeV. The spectra are labelled by the detection angle of the coincident deuterons. The cross sections are normalized to fission singles. The data are fitted with the rotating hot spot model of eq. (3).

Fig. 13. Energy spectra of tritons detected in the reaction ^{238}U (^{16}O, tf) at 315 MeV. The spectra are labelled by the detection angle of the coincident tritons. The cross sections are normalized to fission singles. The data are fitted with the rotating hot spot model of eq. (3).

Fig. 14. Energy spectra of alpha particles detected in the reaction ^{238}U (^{16}O, αf) at 315 MeV. The spectra are labelled by the detection angle of the coincident alpha particles. The cross-sections are normalized to fission singles. The data are fitted with the rotating hot spot model of eq. (3).

Fig. 15. Angular dependence of the temperature T_θ, obtained by fitting the p, d, t and α energy spectra (Figs. 11-14) with the rotating hot spot model.

Fig. 16. Angular dependence of ln $(T_\theta - T_o)$, where $T_o = T_{cn} = 3$ MeV and T_θ is the temperature in MeV (Fig. 15) obtained by fitting the p, d, t and α energy spectra according to the hot spot model. The curve shown has a slope of -0.022 deg.$^{-1}$ and an intercept corresponding to $T_i = 22$ MeV.

Fig. 17. Contour plot of the Lorentz invariant proton cross section. The contours, read inward, are in the ratios 1:4:16:64:128. The experimental data are given by circles. The curves in part a represent the cross sections calculated for thermal emission from two sources, one moving with the beam velocity and the other moving with the compound nucleus velocity (see also solid curves in Fig. 19). The curves in part b describe the emission from a single thermal source moving with slightly less than half the beam velocity (see solid curves in Fig. 20).

Fig. 18. Contour plot of the Lorentz invariant proton cross section. The contours, read inward, are in the ratios 1:4:16:64:128. The curves describe the emission from a single thermal source moving with slightly less than half the beam velocity. The cross sections for "central" collisions are shown in part a, the ones for "peripheral" collisions are shown in part b.

Fig. 19. Energy spectra of protons detected in the reaction ^{238}U (^{16}O, pf) at 315 MeV. The curves have been calculated by assuming contributions from two sources, each given by eq. (10). One source is associated with a projectile-like fragment and the other with a target residue. The details of the two curves are explained in section IV.B.

Fig. 20. Energy spectra of protons detected in the reaction ^{238}U (^{16}O, pf) at 315 MeV. The curves have been calculated with eq. (10).

Fig. 21. Energy spectra of deuterons detected in the reaction ^{238}U (^{16}O, df) at 315 MeV. The curves have been calculated with eq. (10).

Fig. 22. Energy spectra of tritons detected in the reaction ^{238}U (^{16}O, tf) at 315 MeV. The curves have been calculated with eq. (10).

Fig. 23. Energy spectra of alpha particles detected in the reaction ^{238}U (^{16}O, αf) at 315 MeV. The curves have been calculated with eq. (10).

Fig. 24. Energy spectra of deuterons (solid points) detected in the reaction ^{238}U (^{16}O, df) at 315 MeV. The open squares are spectra predicted by the Coulomb-modified coalescence model; the dashed curves are the predictions of the coalescence model if Coulomb effects are neglected.

Fig. 25. Energy spectra of tritons (solid points) detected in the reaction ^{238}U (^{16}O, tf) at 315 MeV. The open squares are spectra predicted by the Coulomb-modified coalescence model.

Fig. 26. Energy spectra of alpha particles (solid points) detected in the reaction ^{238}U (^{16}O, αf) at 315 MeV. The open squares are spectra predicted by the Coulomb-modified coalescence model.

MSUX-80-561

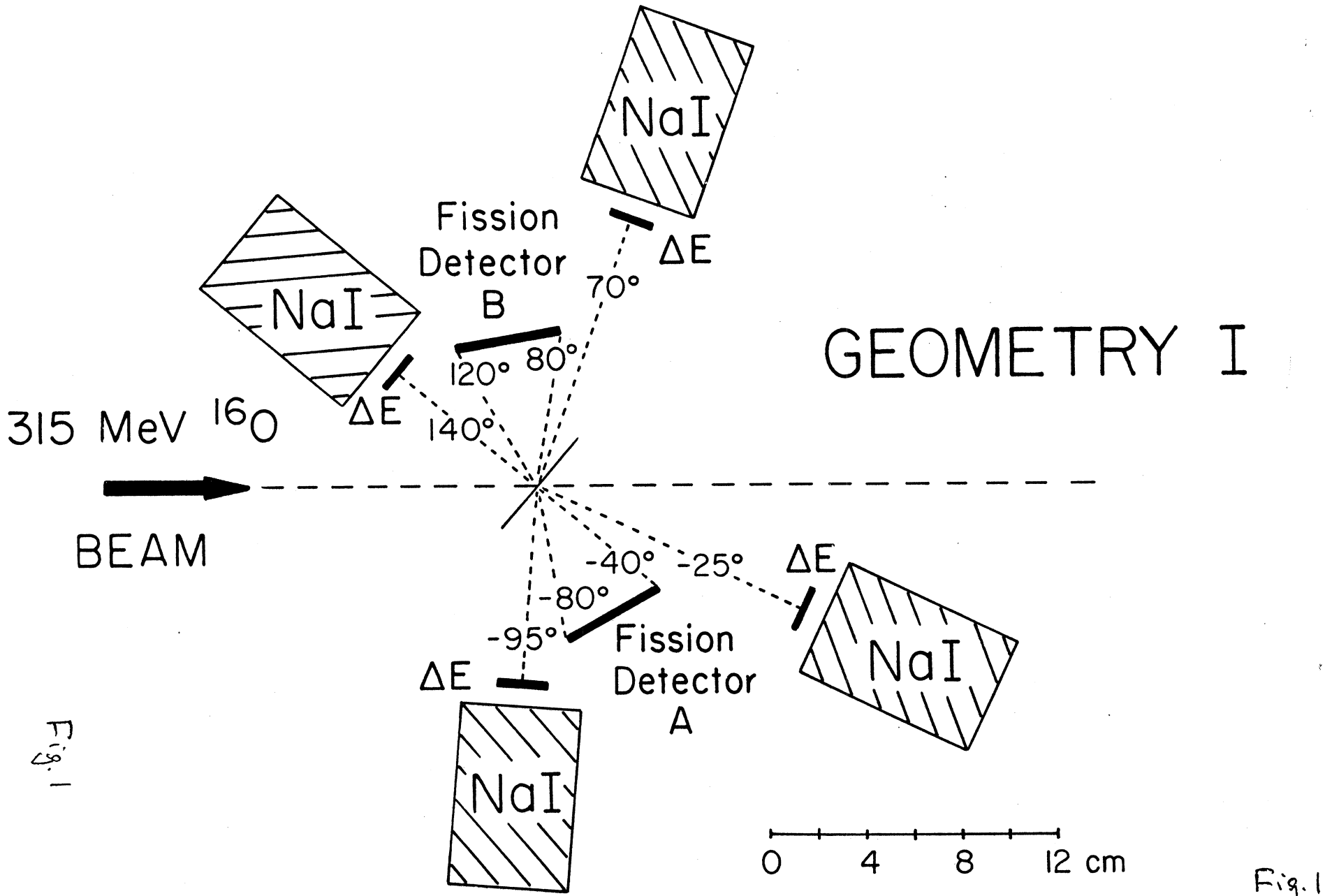

Fig. 1

Fig. 1

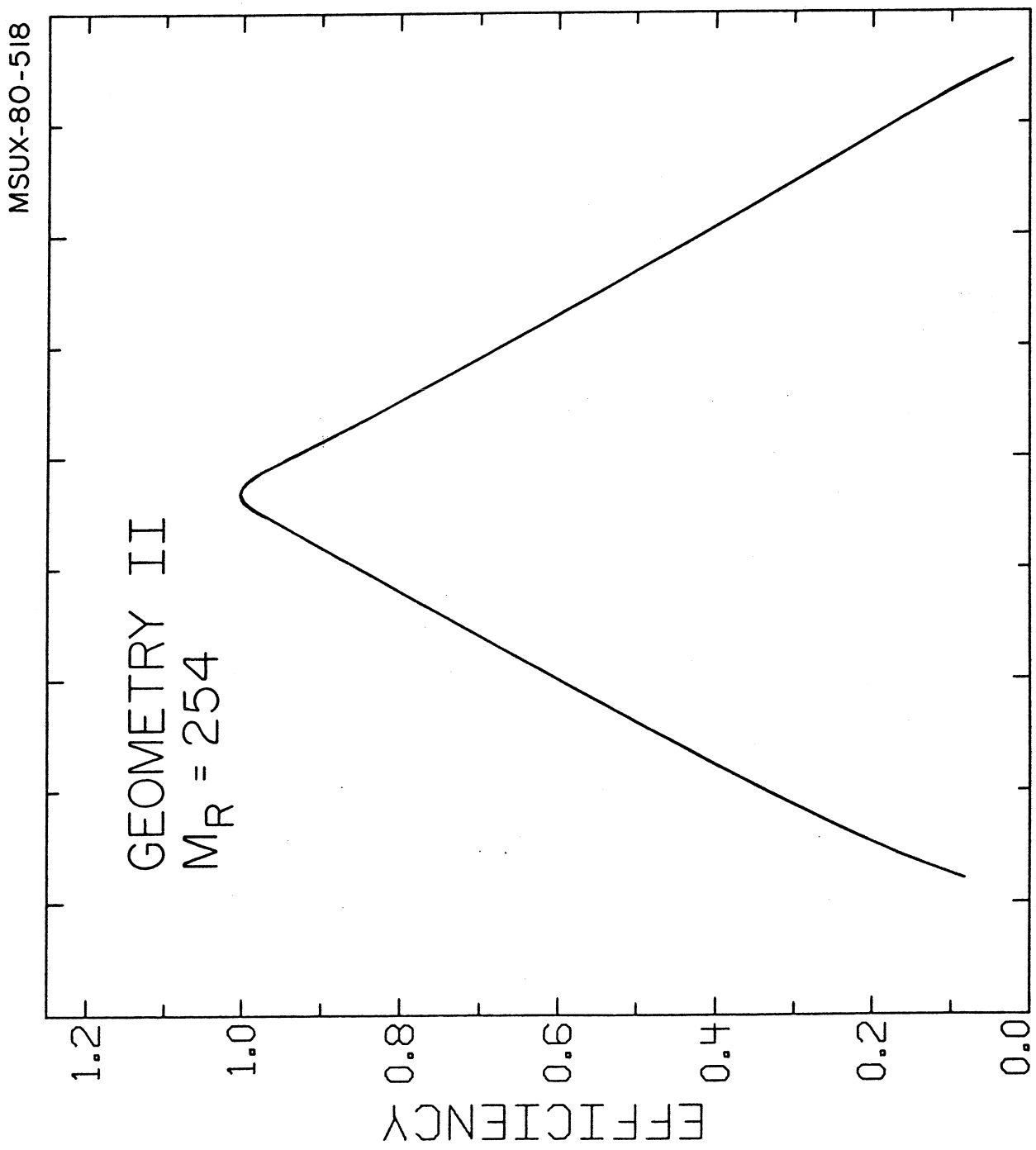
MSUX-80-518
GEOMETRY II
$M_R = 254$
EFFICIENCY
1.2
1.0
0.8
0.6
0.4
0.2
0.0
120
140
160
180
$\langle\theta_{AB}\rangle$ (deg)

Fig. 2

Fig. 2

MSUX-80-515

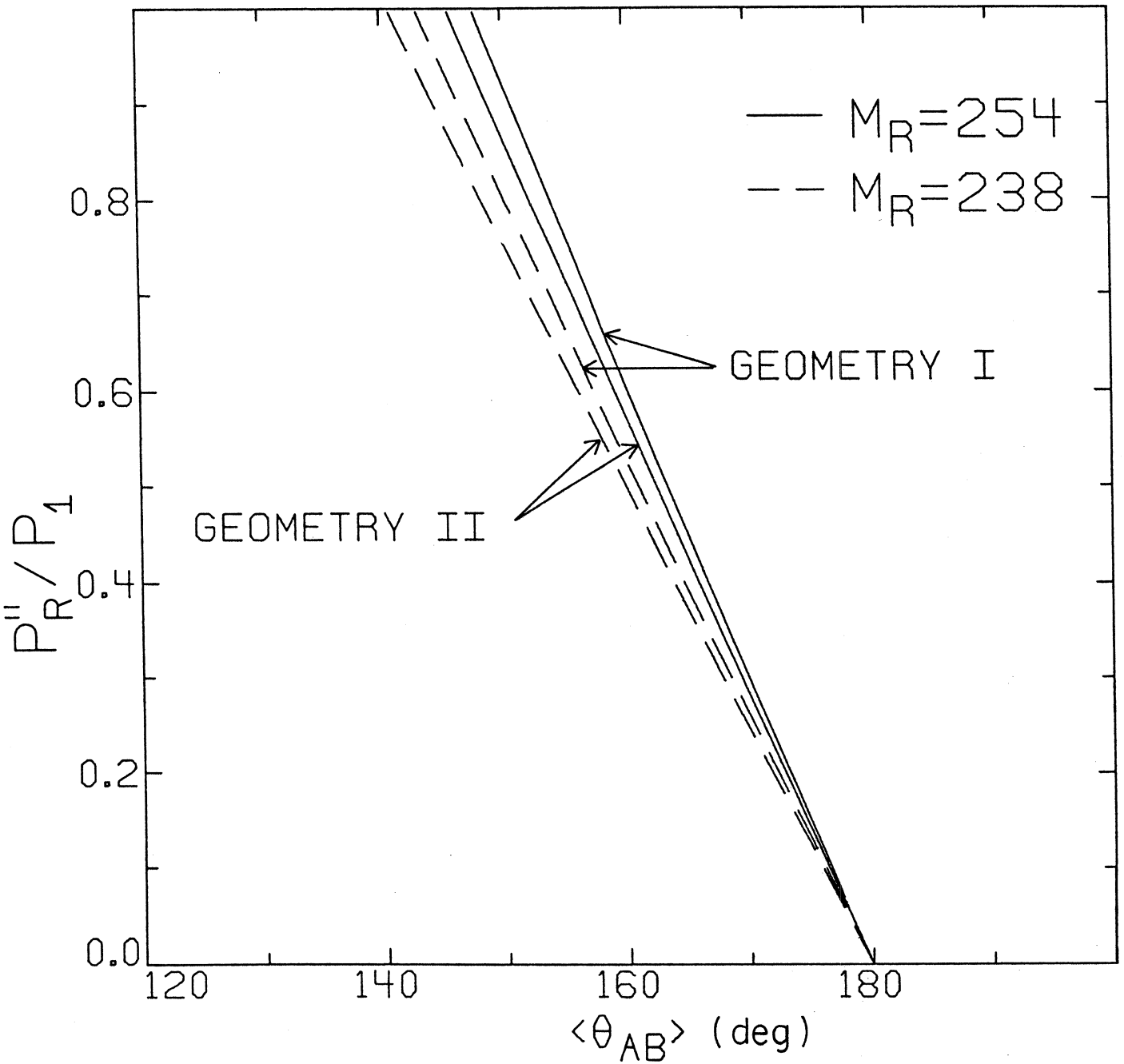

Fig. 3

Fig. 3

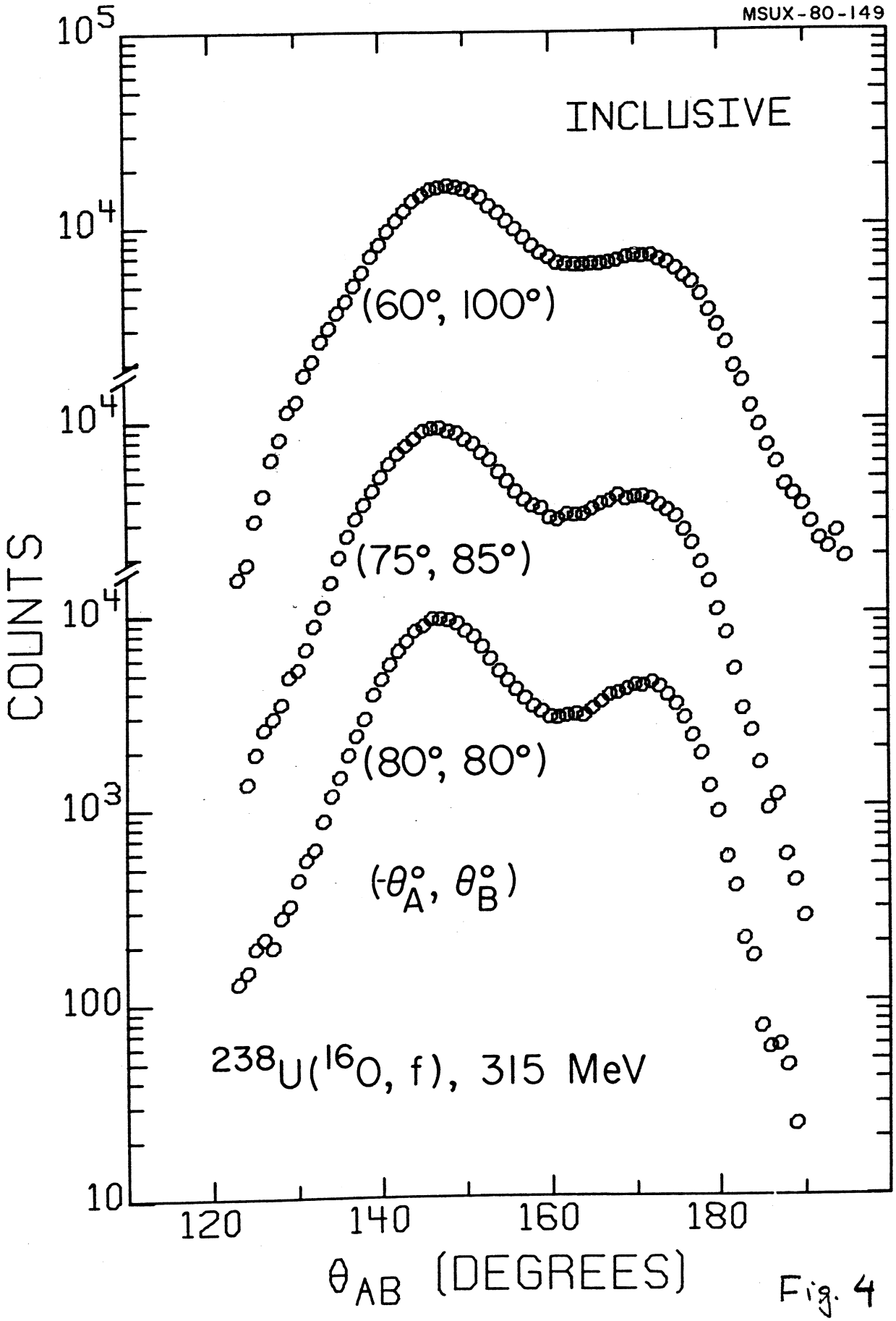
MSUX-80-149
INCLUSIVE
(60°, 100°)
(75°, 85°)
(80°, 80°)
(-θA°, θB°)
238U(16O, f), 315 MeV
COUNTS
θAB (DEGREES)
10^5
10^4
10^4
10^4
10^3
100
10
120
140
160
180

Fig. 4

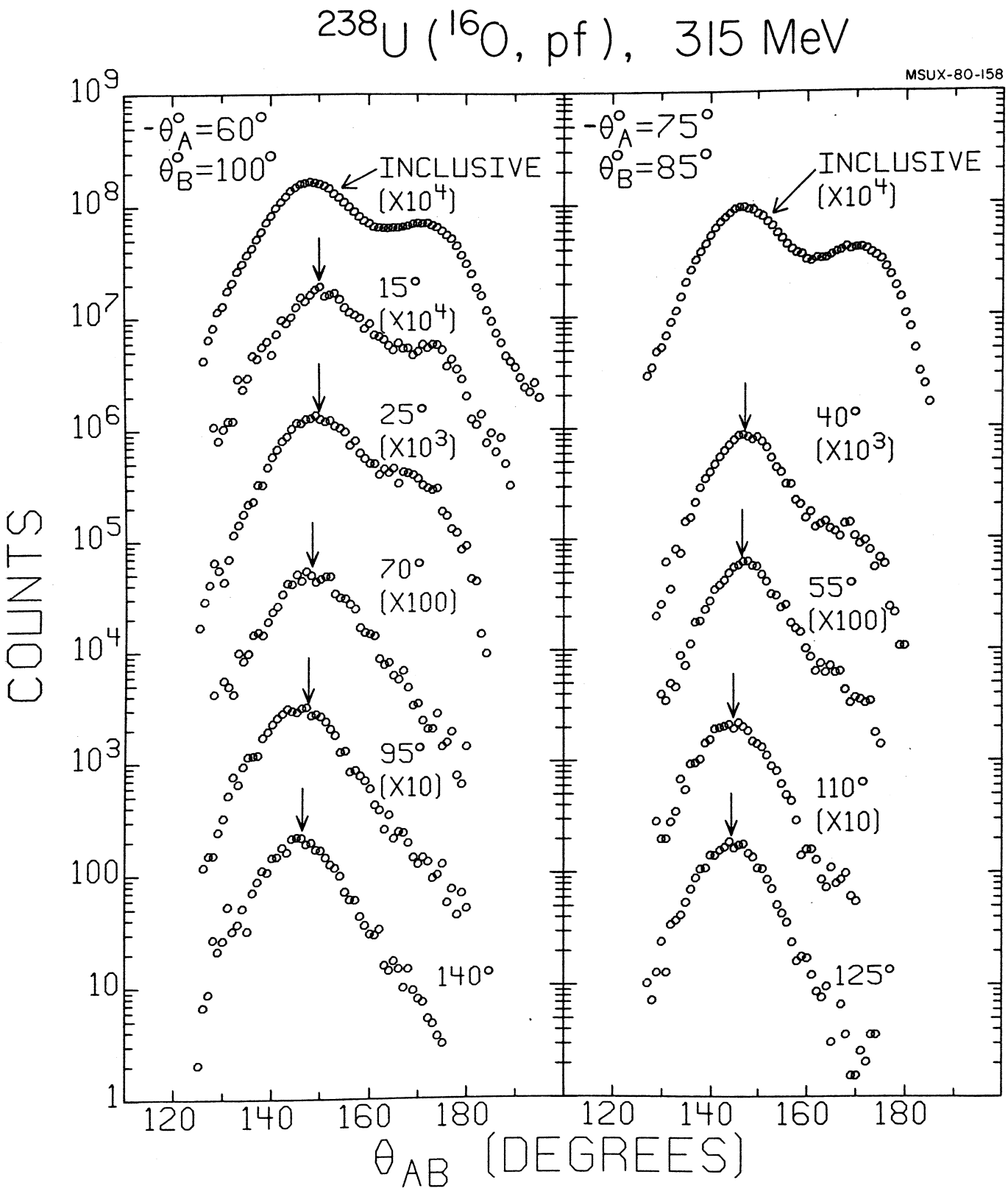
^{238}U (^{16}O, pf), 315 MeV
MSUX-80-158
$-\theta_A^\circ=60^\circ$
$\theta_B^\circ=100^\circ$
INCLUSIVE (X10^4)
15° (X10^4)
25° (X10^3)
70° (X100)
95° (X10)
140°
$-\theta_A^\circ=75^\circ$
$\theta_B^\circ=85^\circ$
INCLUSIVE (X10^4)
40° (X10^3)
55° (X100)
110° (X10)
125°
COUNTS
θ_{AB} (DEGREES)

Fig. 5

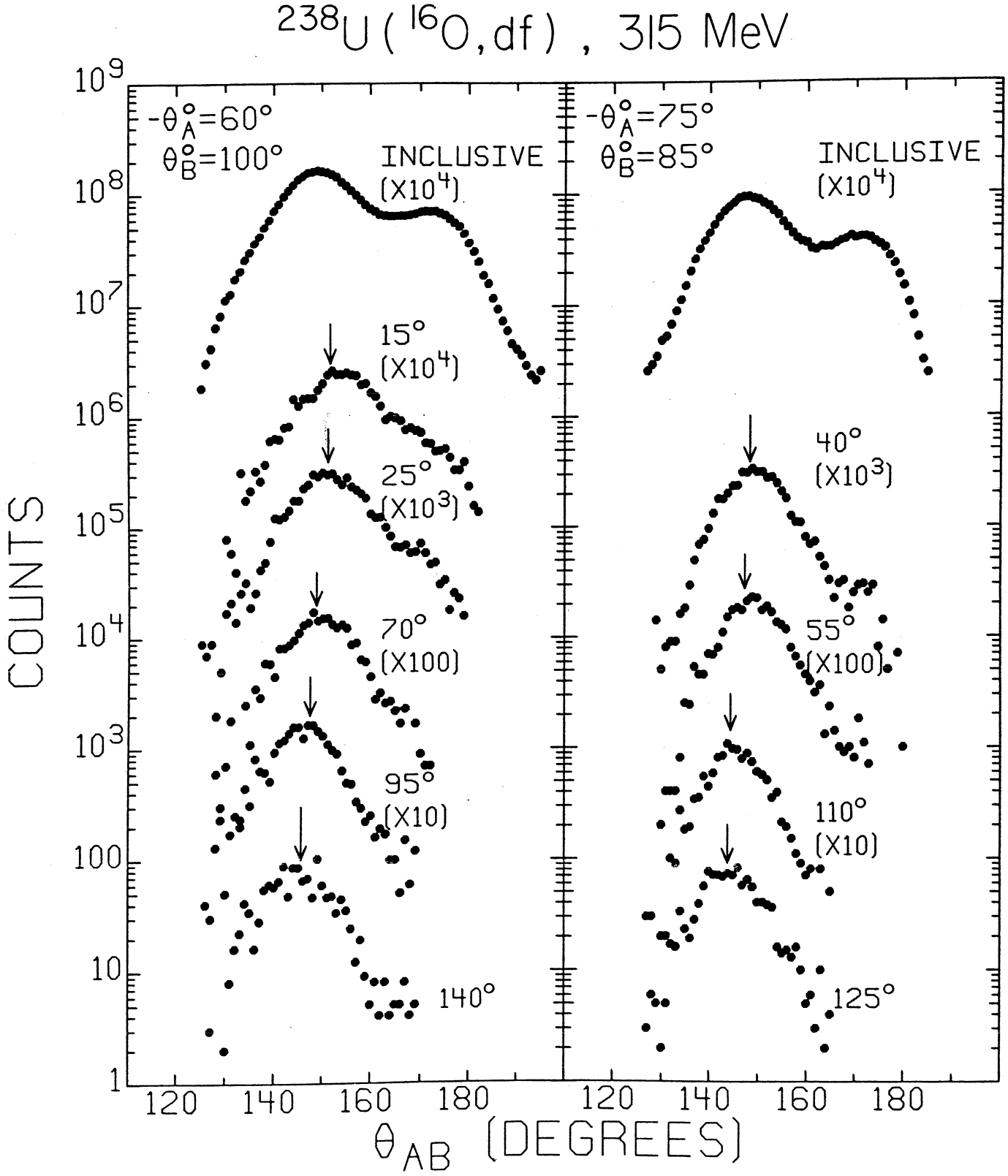
$^{238}U(^{16}O,df)$, 315 MeV
$-\theta_A^\circ=60^\circ$
$\theta_B^\circ=100^\circ$
INCLUSIVE (X10^4)
15° (X10^4)
25° (X10^3)
70° (X100)
95° (X10)
140°
$-\theta_A^\circ=75^\circ$
$\theta_B^\circ=85^\circ$
INCLUSIVE (X10^4)
40° (X10^3)
55° (X100)
110° (X10)
125°
COUNTS
θ_{AB} (DEGREES)

Fig. 6

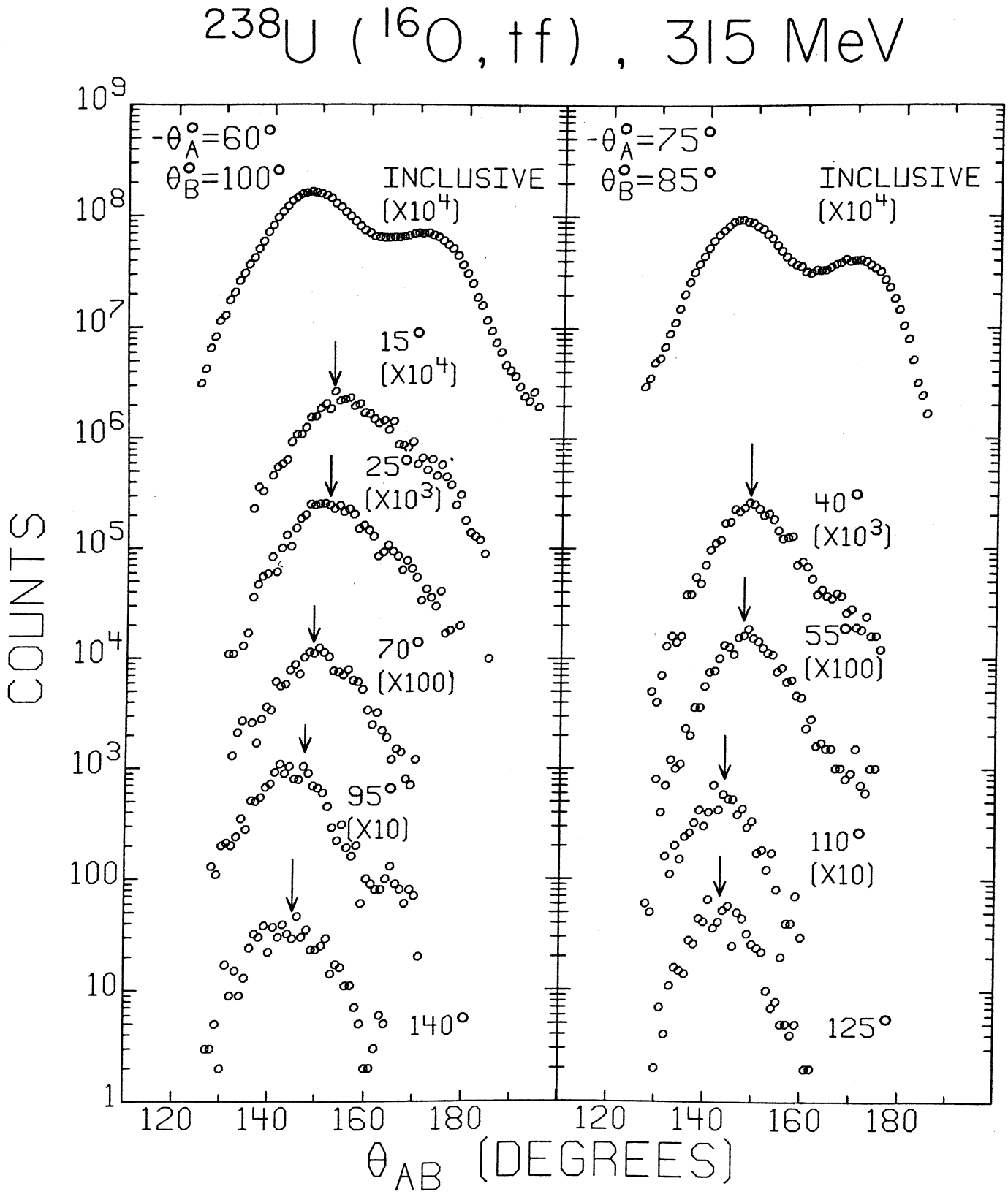
^{238}U (^{16}O, tf), 315 MeV
$-\theta_A^\circ=60^\circ$
$\theta_B^\circ=100^\circ$
INCLUSIVE (X10^4)
15° (X10^4)
25° (X10^3)
70° (X100)
95° (X10)
140°
$-\theta_A^\circ=75^\circ$
$\theta_B^\circ=85^\circ$
INCLUSIVE (X10^4)
40° (X10^3)
55° (X100)
110° (X10)
125°
COUNTS
θ_{AB} (DEGREES)

Fig. 7

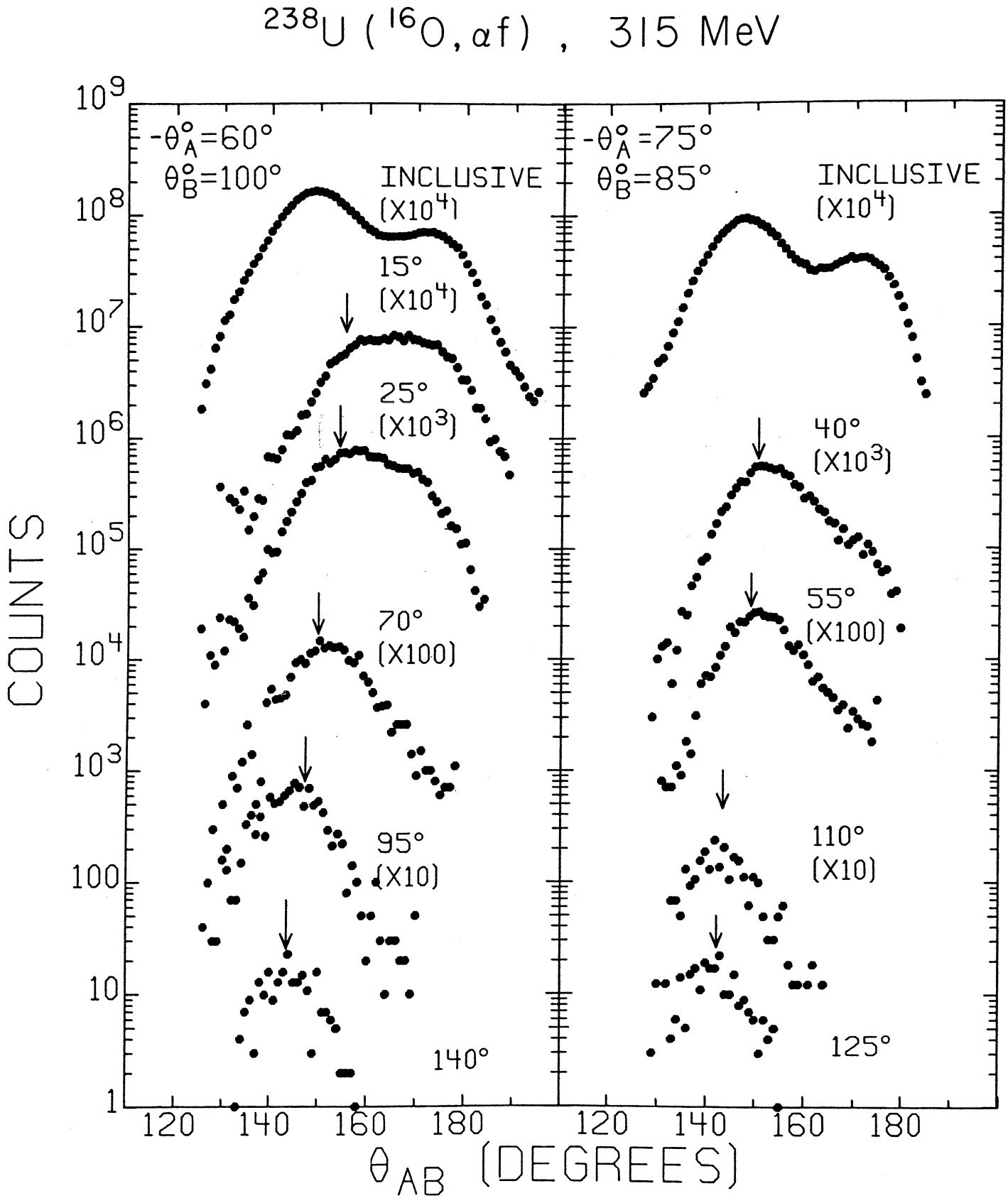
^{238}U (^{16}O, αf) , 315 MeV
$-\theta_A^\circ=60^\circ$
$\theta_B^\circ=100^\circ$
INCLUSIVE (X10^4)
15° (X10^4)
25° (X10^3)
70° (X100)
95° (X10)
140°
$-\theta_A^\circ=75^\circ$
$\theta_B^\circ=85^\circ$
INCLUSIVE (X10^4)
40° (X10^3)
55° (X100)
110° (X10)
125°
COUNTS
θ_{AB} (DEGREES)

Fig. 8

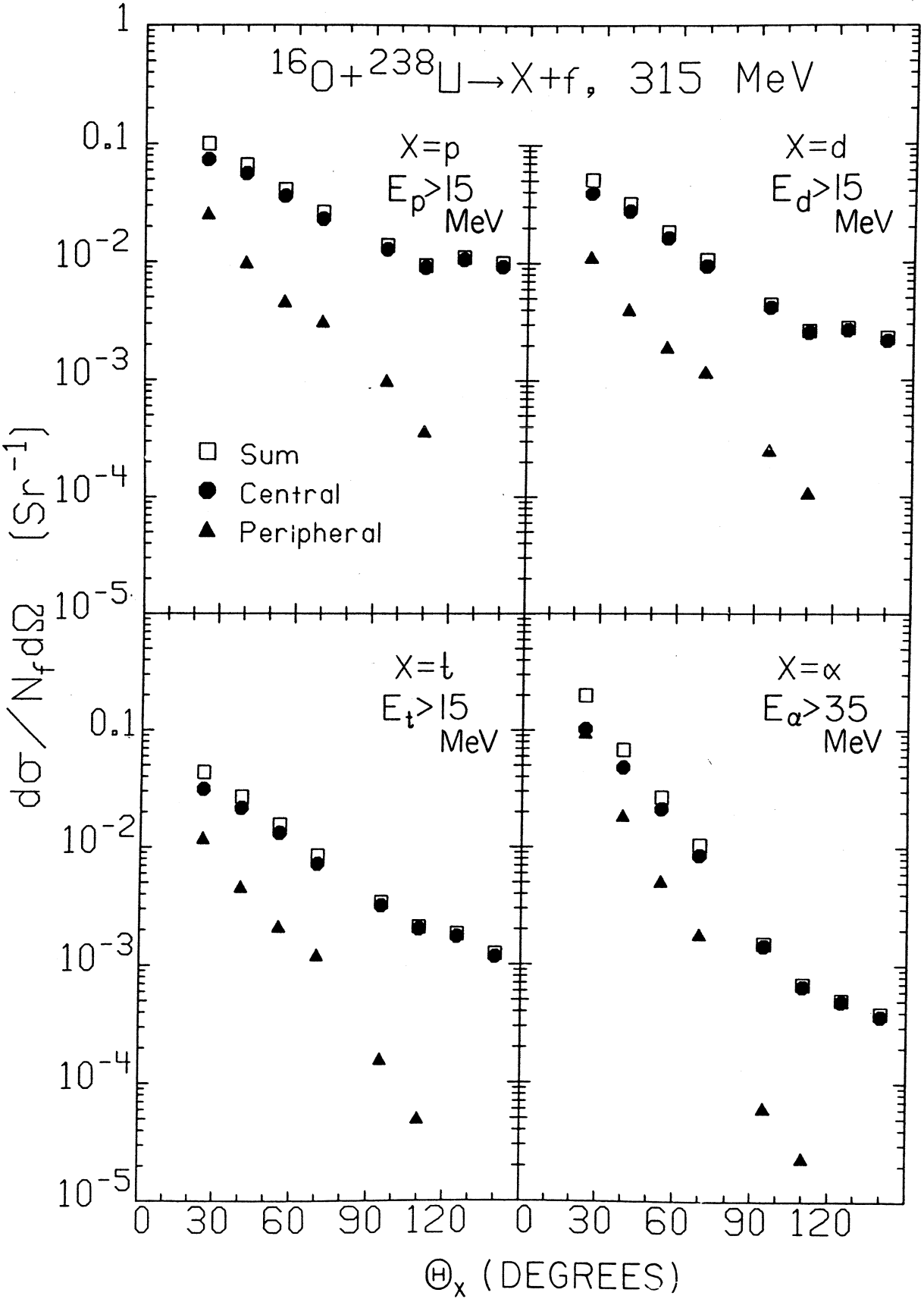
$^{16}O+^{238}U \rightarrow X+f$, 315 MeV
X=p
E_p>15 MeV
X=d
E_d>15 MeV
X=t
E_t>15 MeV
X=α
E_α>35 MeV
Sum
Central
Peripheral
$d\sigma / N_f d\Omega$ (Sr^{-1})
1
0.1
10^{-2}
10^{-3}
10^{-4}
10^{-5}
0 30 60 90 120
Θ_x (DEGREES)

Fig. 9

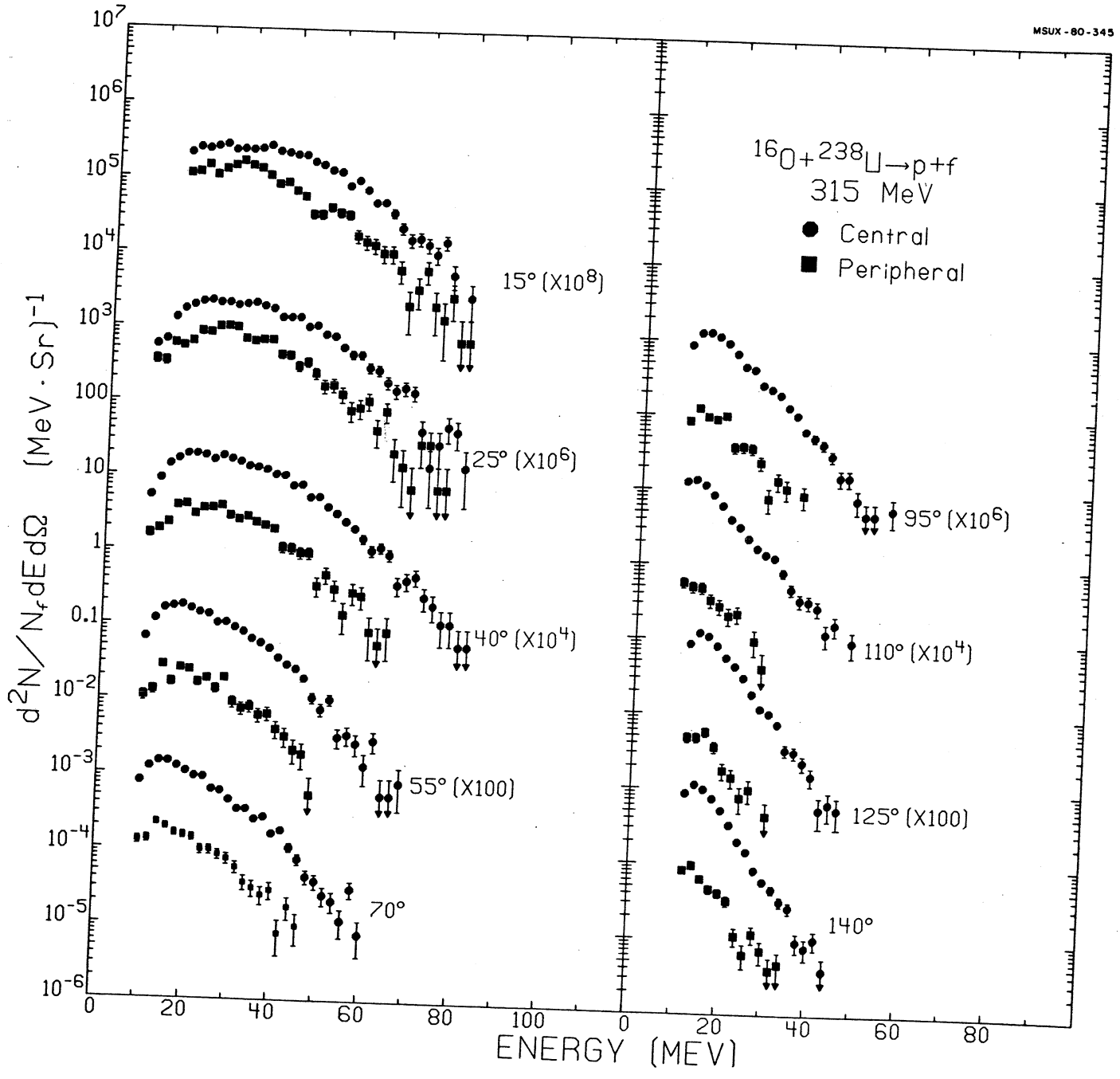
MSUX-80-345
$^{16}O+^{238}U \rightarrow p+f$
315 MeV
Central
Peripheral
15° (X10⁸)
25° (X10⁶)
40° (X10⁴)
55° (X100)
70°
95° (X10⁶)
110° (X10⁴)
125° (X100)
140°
$d^2N/N_f dE d\Omega$ (MeV · Sr)⁻¹
ENERGY (MEV)

Fig. 10

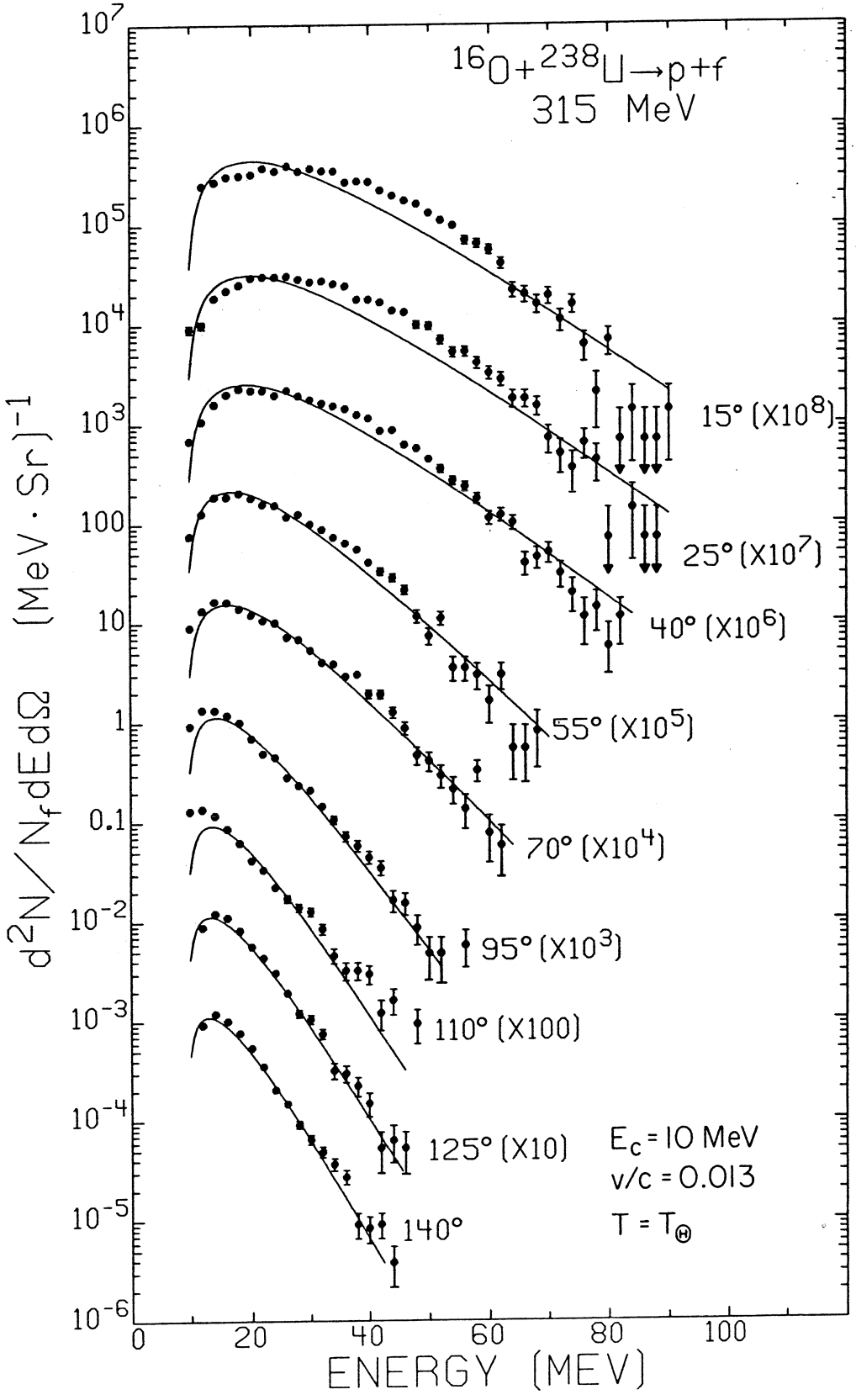
$^{16}O+^{238}U \rightarrow p+f$
315 MeV
15° (X10^8)
25° (X10^7)
40° (X10^6)
55° (X10^5)
70° (X10^4)
95° (X10^3)
110° (X100)
125° (X10)
140°
E_c = 10 MeV
v/c = 0.013
T = T_Θ
$d^2N/N_f dE d\Omega$ (MeV · Sr)$^{-1}$
ENERGY (MEV)

Fig. 11

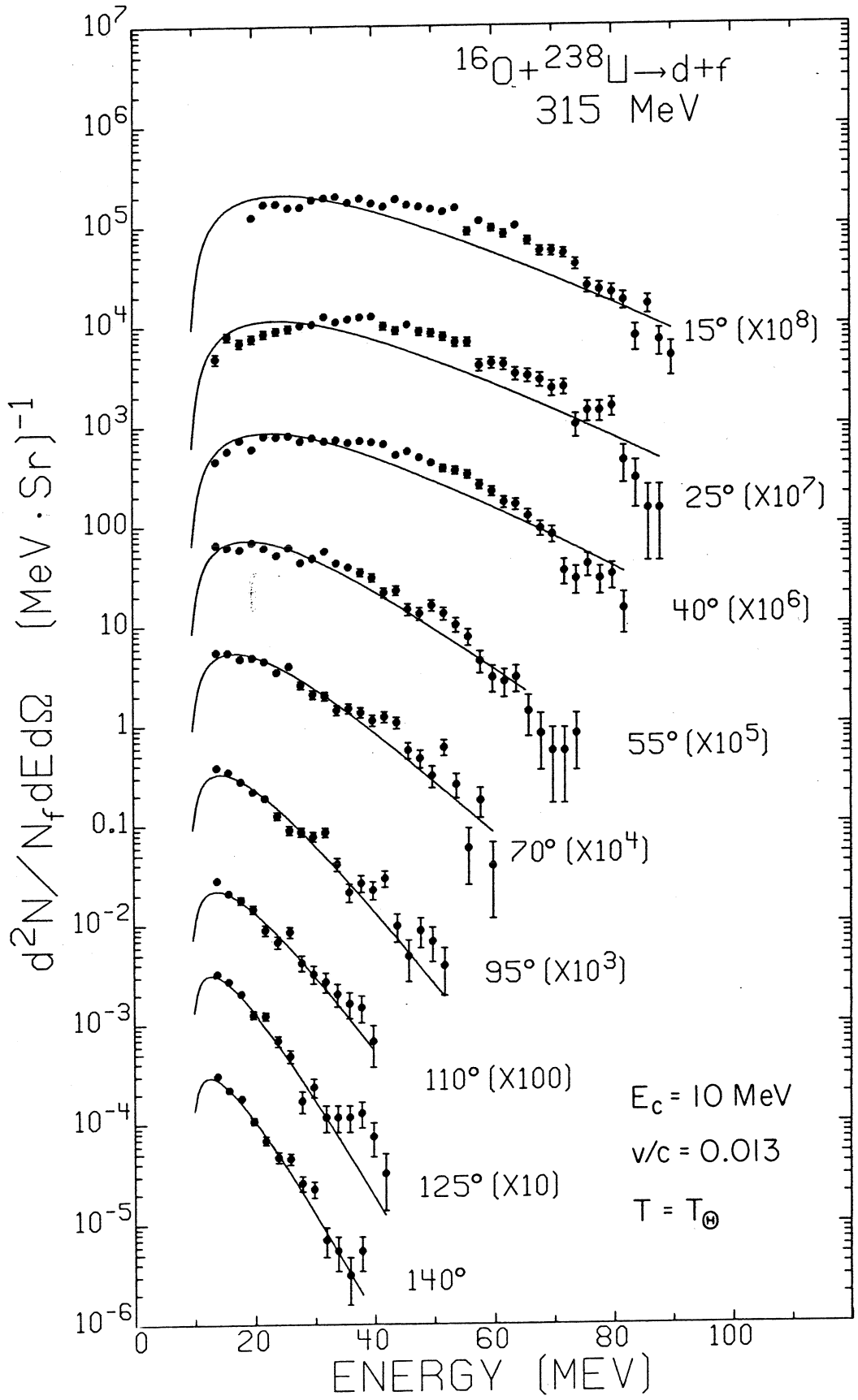
$^{16}O+^{238}U \rightarrow d+f$
315 MeV
15° (X10^8)
25° (X10^7)
40° (X10^6)
55° (X10^5)
70° (X10^4)
95° (X10^3)
110° (X100)
125° (X10)
140°
E_c = 10 MeV
v/c = 0.013
$T = T_\Theta$
$d^2N/N_f dE d\Omega$ (MeV · Sr)$^{-1}$
ENERGY (MEV)

Fig. 12

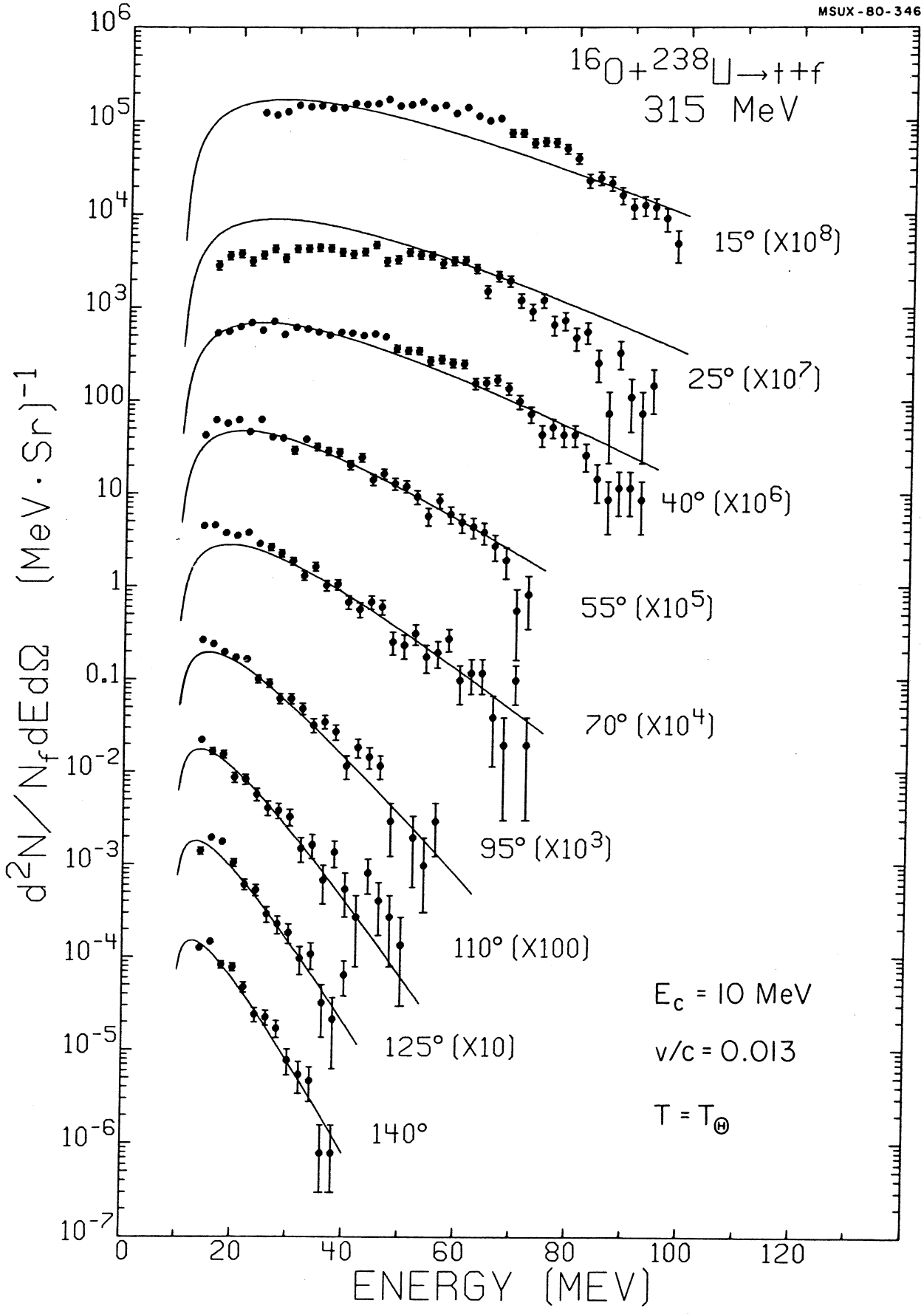
MSUX-80-346
$^{16}O+^{238}U \rightarrow t+f$
315 MeV
15° (X10^8)
25° (X10^7)
40° (X10^6)
55° (X10^5)
70° (X10^4)
95° (X10^3)
110° (X100)
125° (X10)
140°
E_c = 10 MeV
v/c = 0.013
$T = T_{\Theta}$
$d^2N/N_f dE d\Omega$ (MeV · Sr)$^{-1}$
ENERGY (MEV)
10^6
10^5
10^4
10^3
100
10
1
0.1
10^{-2}
10^{-3}
10^{-4}
10^{-5}
10^{-6}
10^{-7}
0
20
40
60
80
100
120

Fig. 13

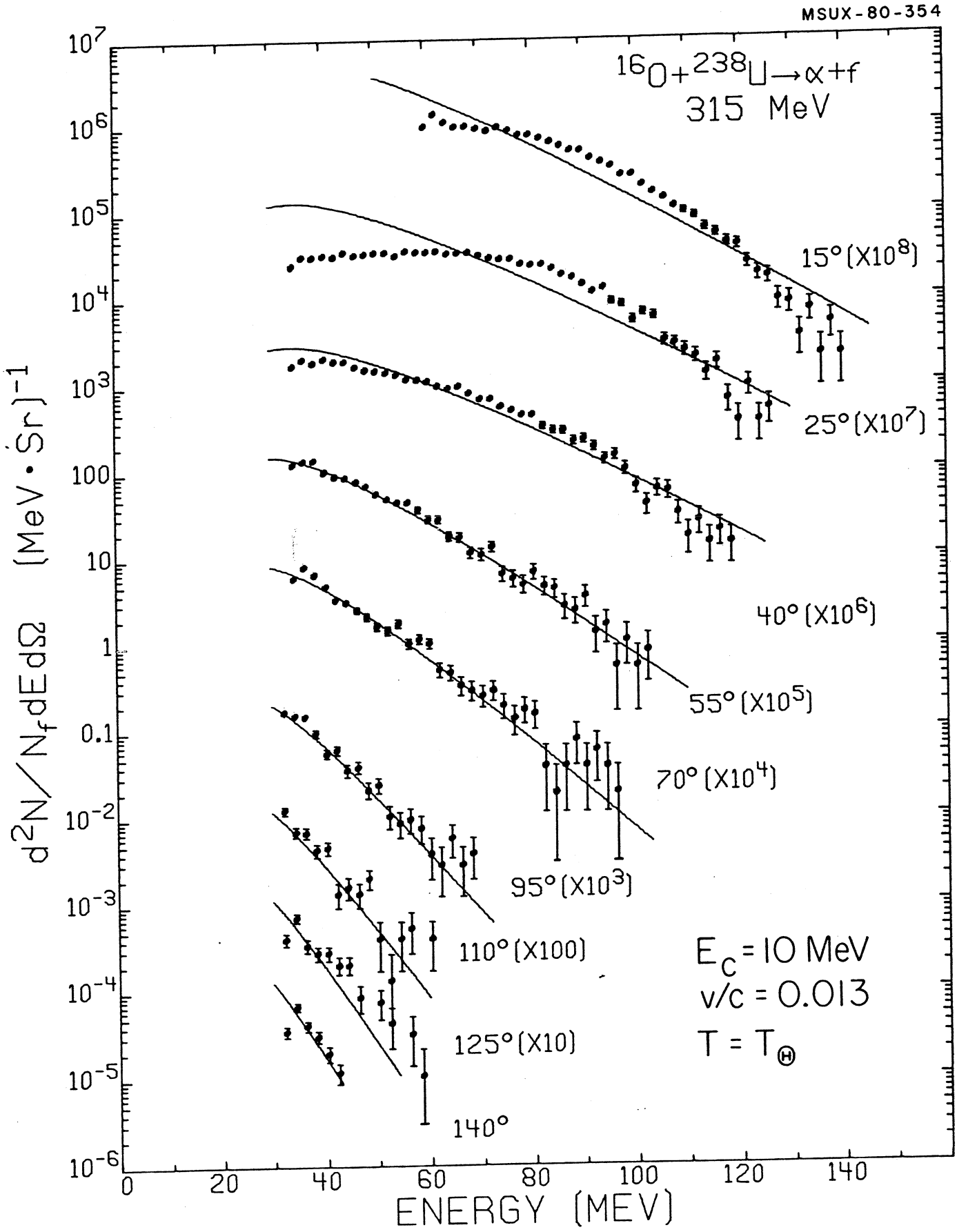
MSUX-80-354
$^{16}O+^{238}U \rightarrow \alpha+f$
315 MeV
15° (X10^8)
25° (X10^7)
40° (X10^6)
55° (X10^5)
70° (X10^4)
95° (X10^3)
110° (X100)
125° (X10)
140°
E_c = 10 MeV
v/c = 0.013
$T = T_{\odot}$
$d^2N/N_f dE d\Omega$ (MeV · Sr)$^{-1}$
ENERGY (MEV)

Fig. 14

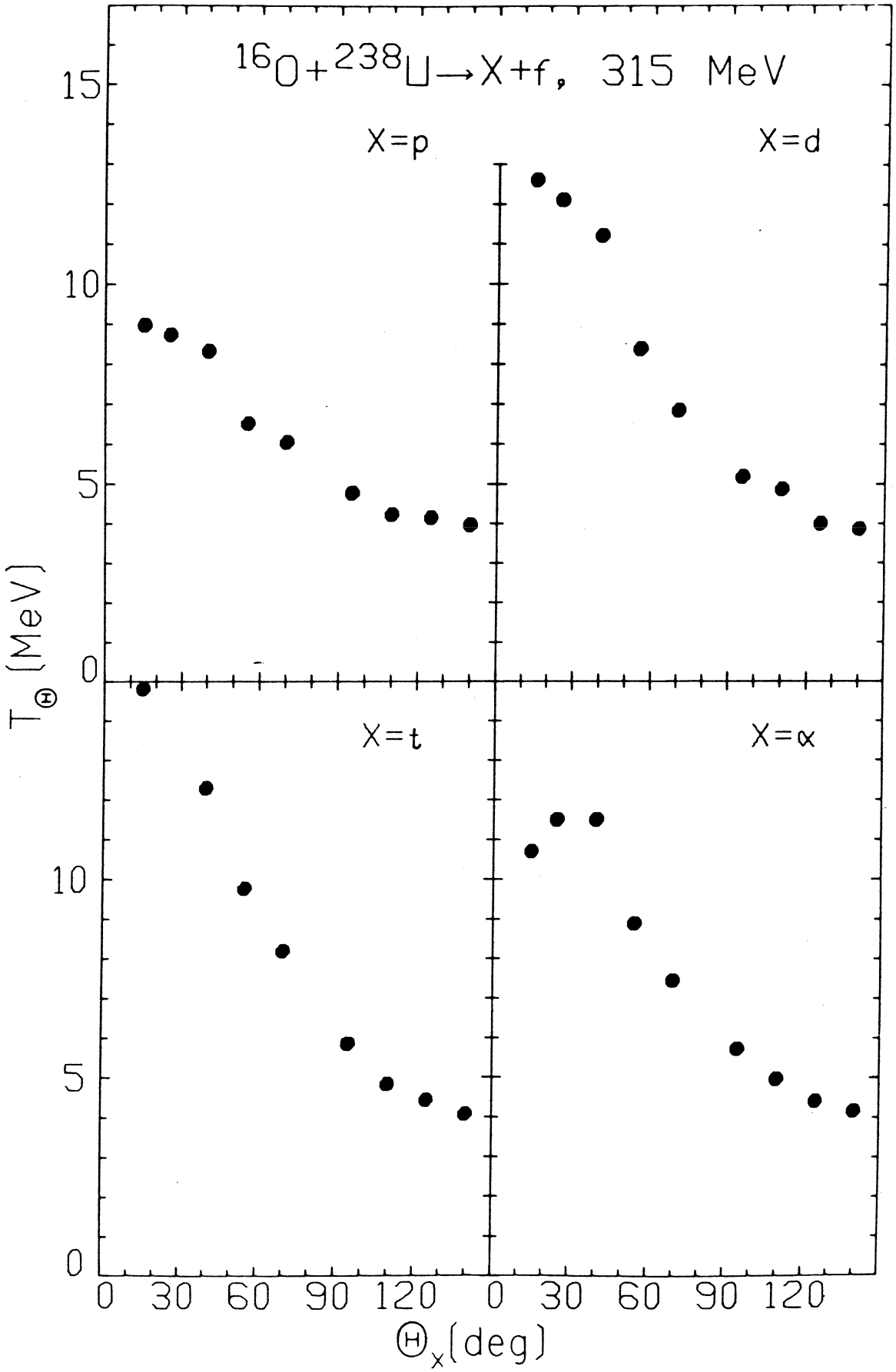
$^{16}O+^{238}U \rightarrow X+f$, 315 MeV
X=p
X=d
X=t
X=α
T_Θ (MeV)
Θ_X (deg)
0
5
10
15
0 30 60 90 120

Fig. 15

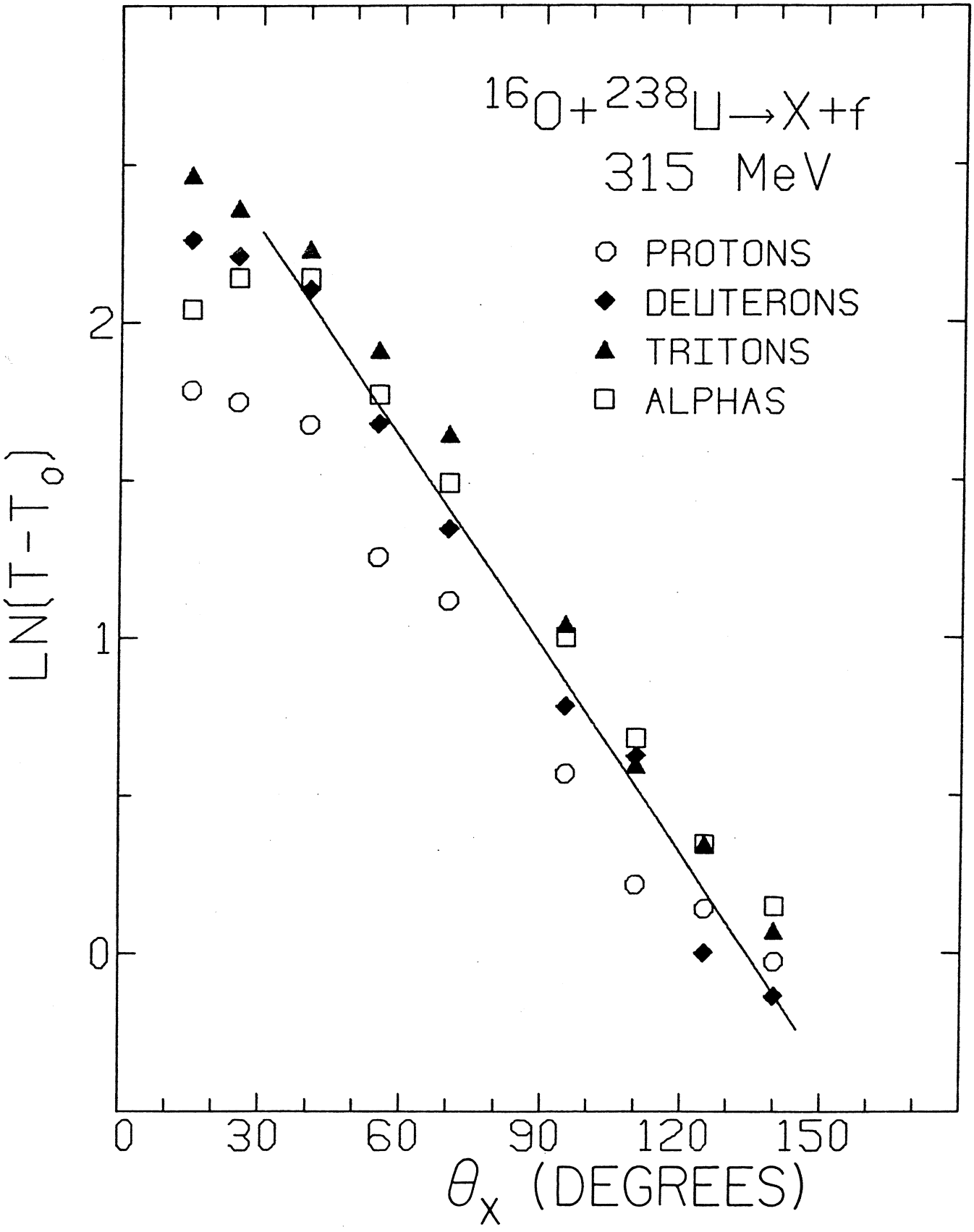
$^{16}O+^{238}U \rightarrow X+f$
315 MeV
PROTONS
DEUTERONS
TRITONS
ALPHAS
LN(T-T$_o$)
2
1
0
0
30
60
90
120
150
θ_X (DEGREES)

Fig. 16

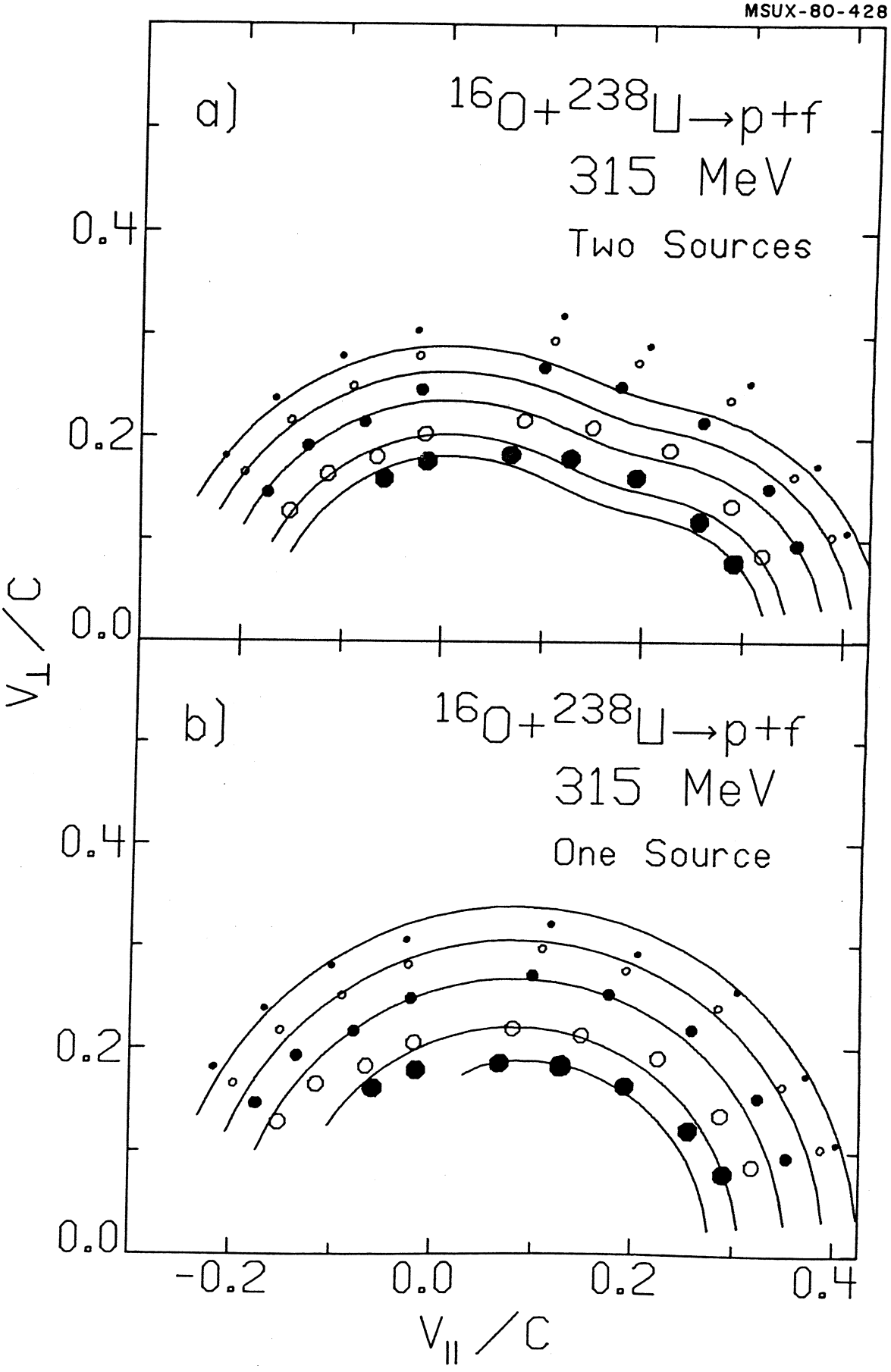
a)
$^{16}O+^{238}U \rightarrow p+f$
315 MeV
Two Sources
b)
$^{16}O+^{238}U \rightarrow p+f$
315 MeV
One Source
0.4
0.2
0.0
-0.2
0.0
0.2
0.4
$V_\perp / C$
$V_{||} / C$

Fig. 17

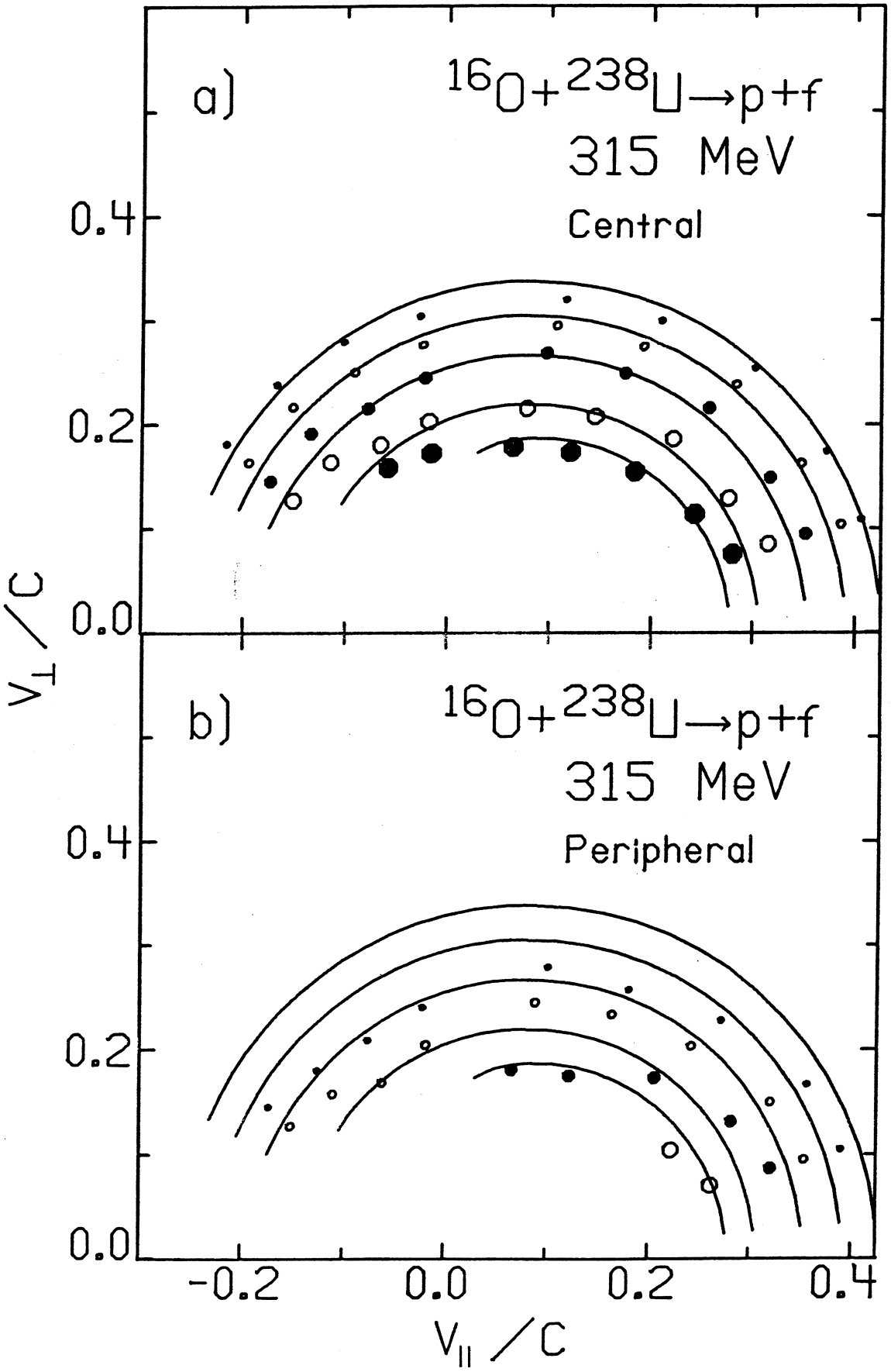
a)
$^{16}O+^{238}U \rightarrow p+f$
315 MeV
Central
b)
$^{16}O+^{238}U \rightarrow p+f$
315 MeV
Peripheral
0.4
0.2
0.0
-0.2
0.0
0.2
0.4
$V_\perp / C$
$V_{||} / C$

Fig. 18

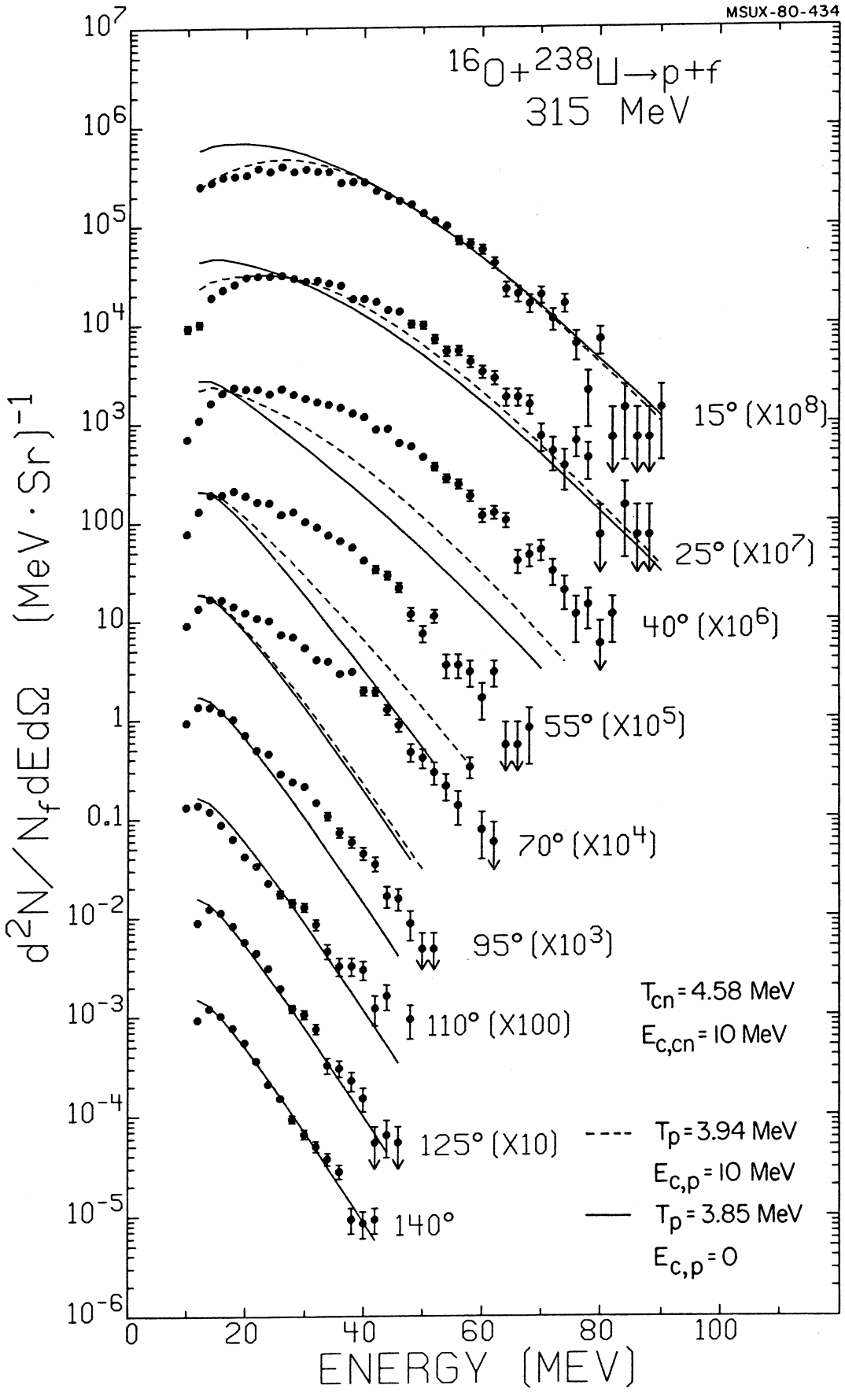
MSUX-80-434
$^{16}O+^{238}U \rightarrow p+f$
315 MeV
$d^2N/N_f dE d\Omega$ (MeV · Sr)$^{-1}$
15° (X10^8)
25° (X10^7)
40° (X10^6)
55° (X10^5)
70° (X10^4)
95° (X10^3)
110° (X100)
125° (X10)
140°
T_{cn} = 4.58 MeV
$E_{c,cn}$ = 10 MeV
T_p = 3.94 MeV
$E_{c,p}$ = 10 MeV
T_p = 3.85 MeV
$E_{c,p}$ = 0
ENERGY (MEV)

Fig. 19

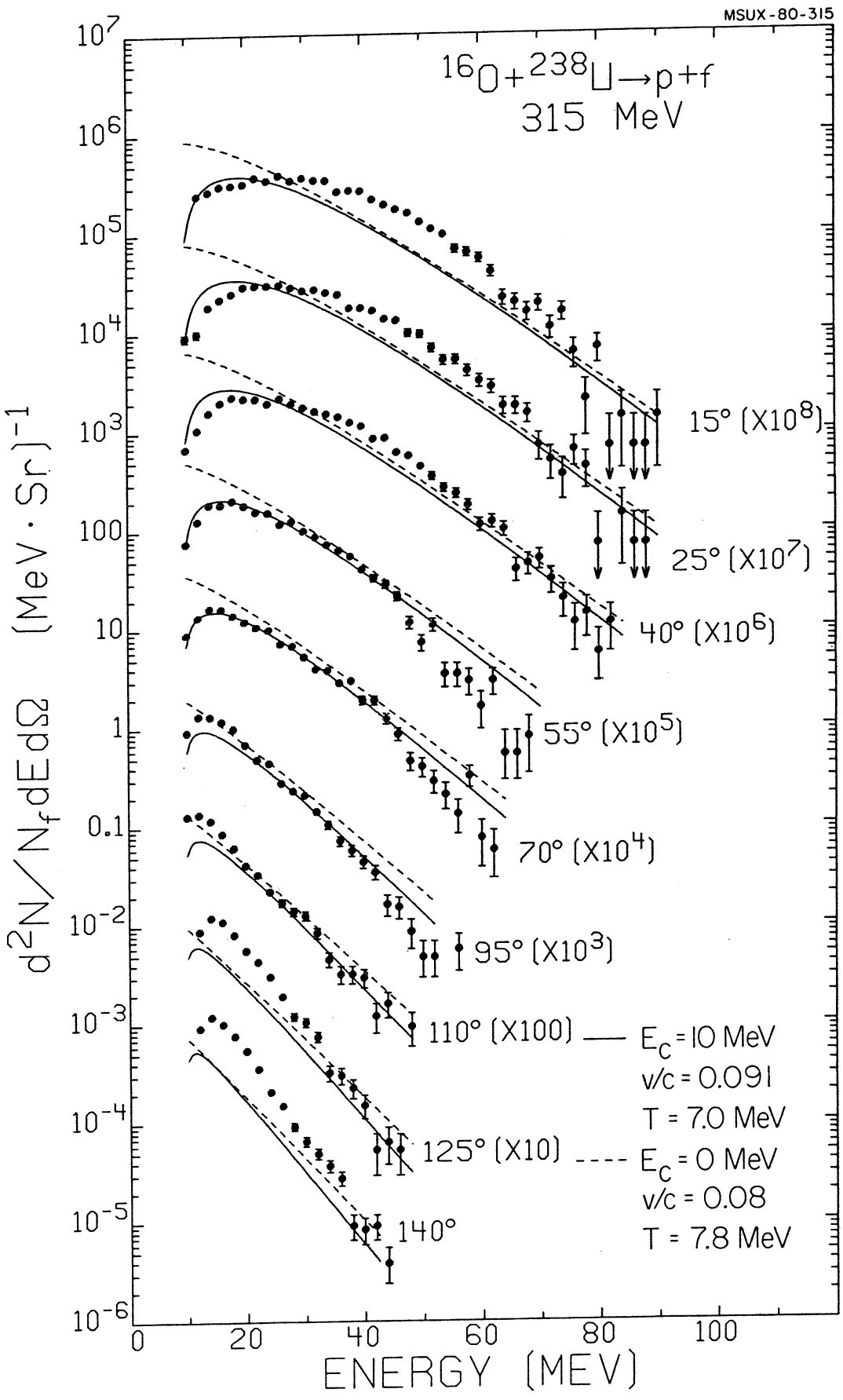
MSUX-80-315
$^{16}O+^{238}U \rightarrow p+f$
315 MeV
$d^2N/N_f dE d\Omega$ (MeV · Sr)$^{-1}$
15° (X10^8)
25° (X10^7)
40° (X10^6)
55° (X10^5)
70° (X10^4)
95° (X10^3)
110° (X100)
125° (X10)
140°
E_C = 10 MeV
v/c = 0.091
T = 7.0 MeV
E_C = 0 MeV
v/c = 0.08
T = 7.8 MeV
ENERGY (MEV)

Fig. 20

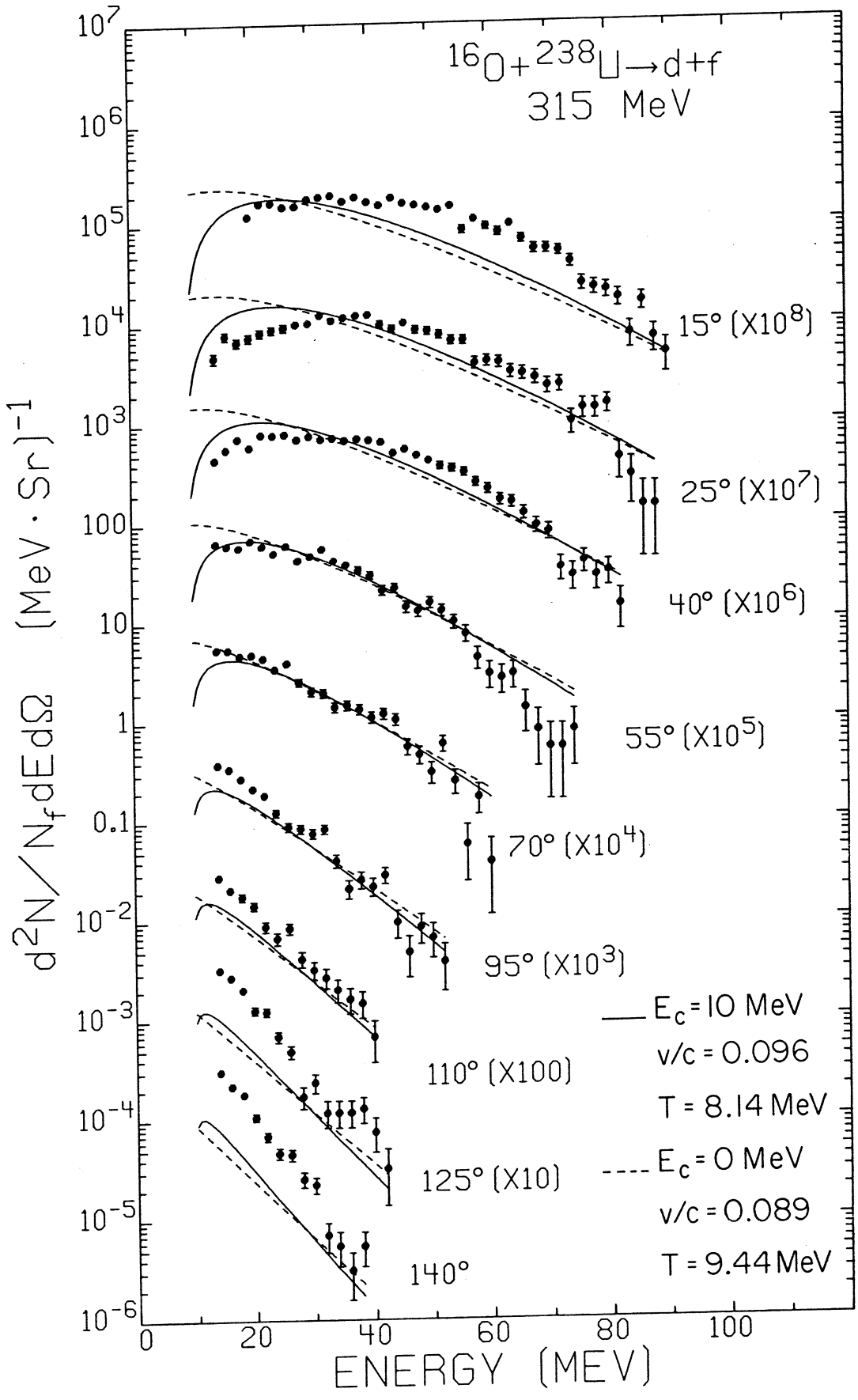
$^{16}O + ^{238}U \rightarrow d + f$
315 MeV
15° (X10^8)
25° (X10^7)
40° (X10^6)
55° (X10^5)
70° (X10^4)
95° (X10^3)
110° (X100)
125° (X10)
140°
E_c = 10 MeV
v/c = 0.096
T = 8.14 MeV
E_c = 0 MeV
v/c = 0.089
T = 9.44 MeV
$d^2N/N_f dE d\Omega$ (MeV · Sr)$^{-1}$
ENERGY (MEV)

Fig. 21

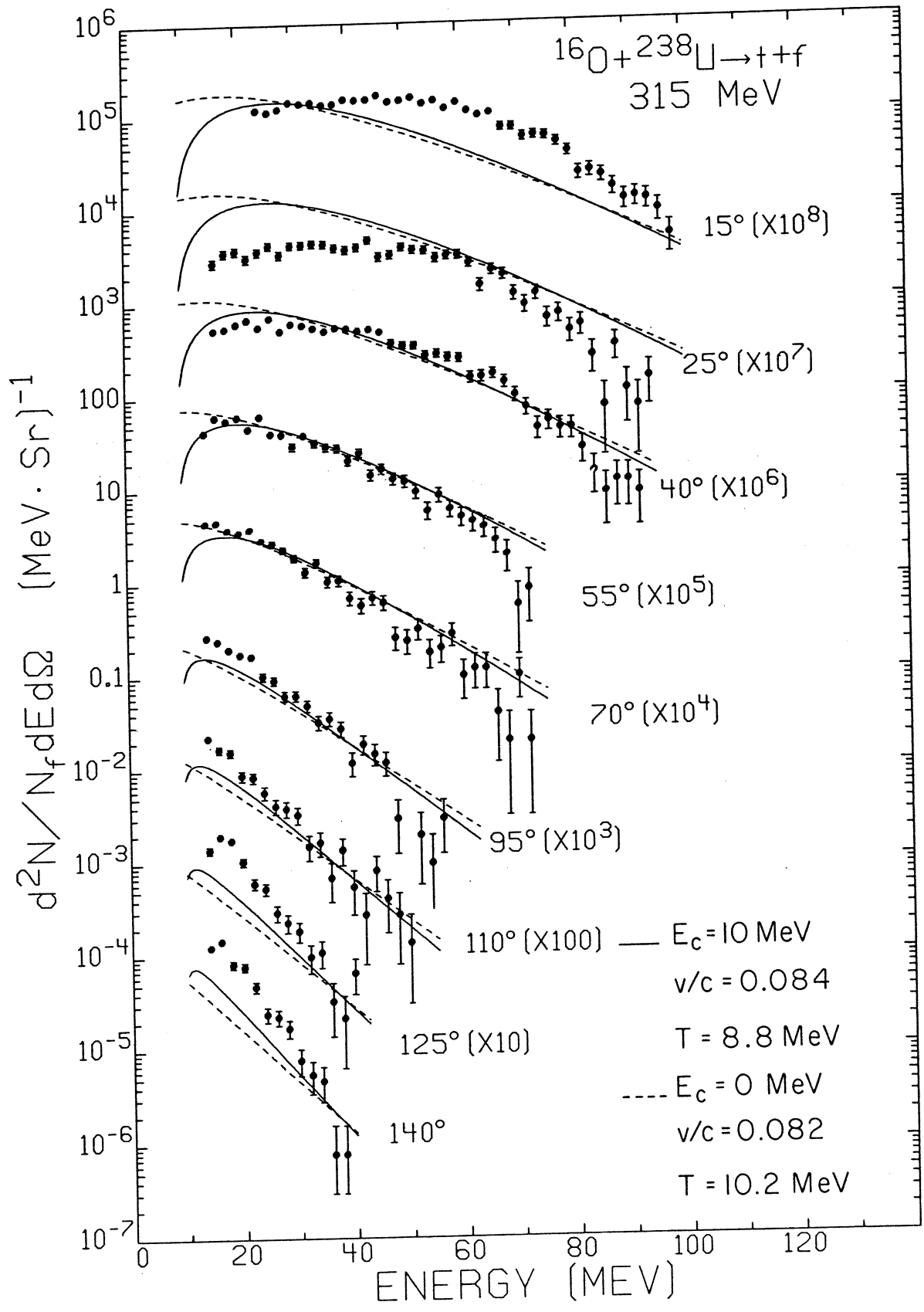
$^{16}O + ^{238}U \rightarrow t + f$
315 MeV
15° (X10^8)
25° (X10^7)
40° (X10^6)
55° (X10^5)
70° (X10^4)
95° (X10^3)
110° (X100)
125° (X10)
140°
E_c = 10 MeV
v/c = 0.084
T = 8.8 MeV
E_c = 0 MeV
v/c = 0.082
T = 10.2 MeV
$d^2N/N_f dE d\Omega$ (MeV · Sr)$^{-1}$
ENERGY (MEV)

Fig. 22

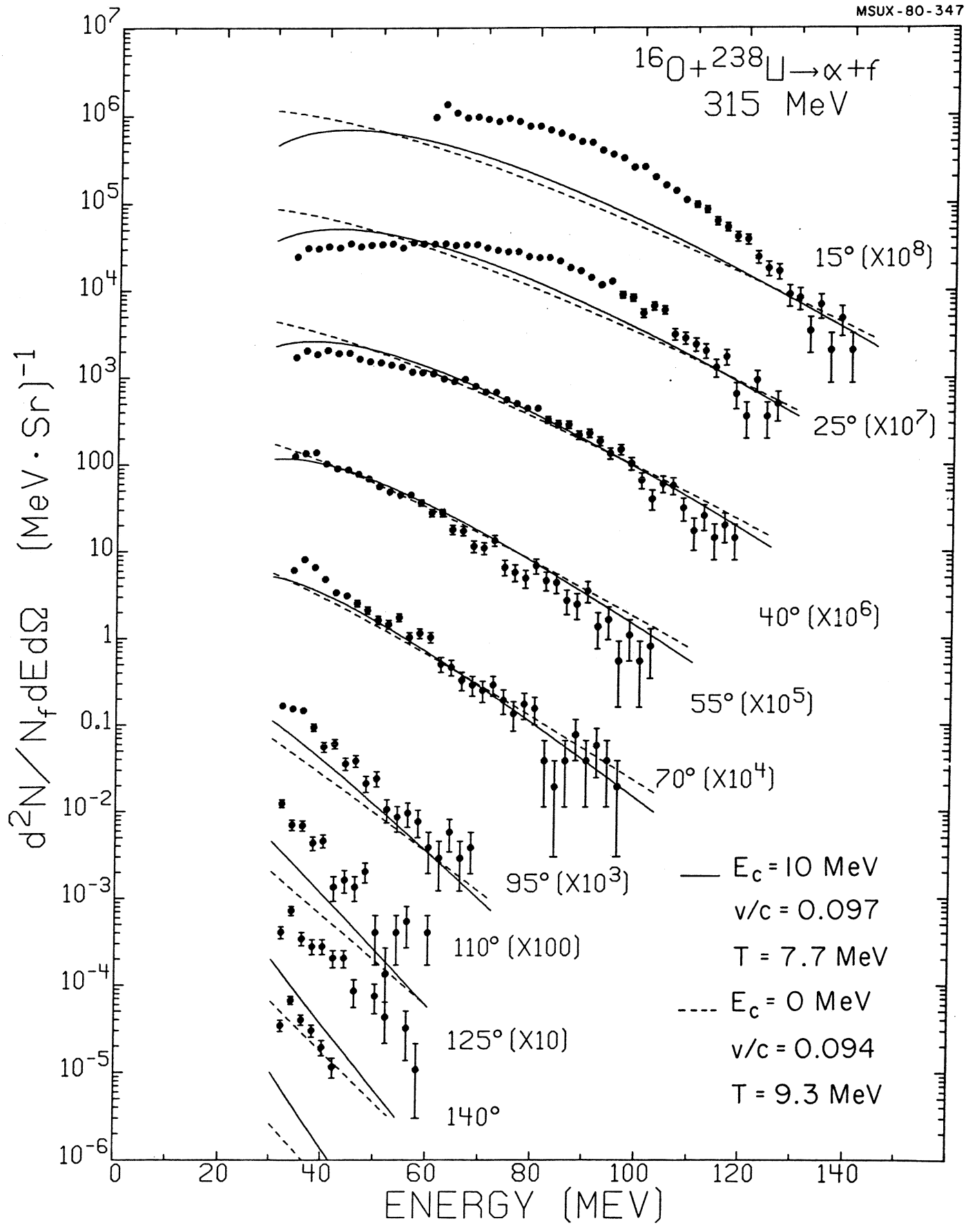
MSUX-80-347
$^{16}O+^{238}U \rightarrow \alpha+f$
315 MeV
15° (X10^8)
25° (X10^7)
40° (X10^6)
55° (X10^5)
70° (X10^4)
95° (X10^3)
110° (X100)
125° (X10)
140°
E_c = 10 MeV
v/c = 0.097
T = 7.7 MeV
E_c = 0 MeV
v/c = 0.094
T = 9.3 MeV
$d^2N/N_f dE d\Omega$ (MeV · Sr)$^{-1}$
ENERGY (MEV)

Fig. 23

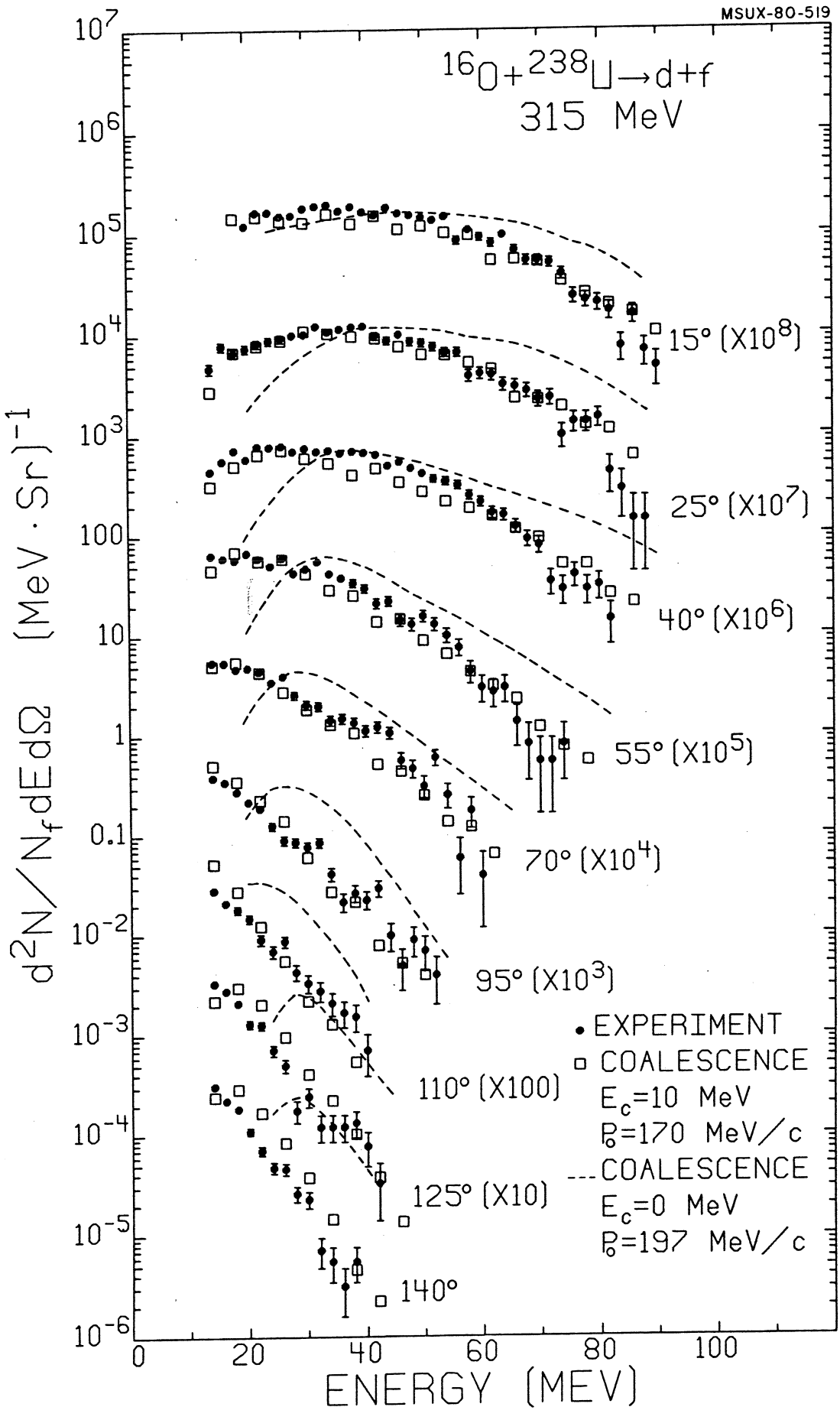
MSUX-80-519
$^{16}O+^{238}U \rightarrow d+f$
315 MeV
15° (X10^8)
25° (X10^7)
40° (X10^6)
55° (X10^5)
70° (X10^4)
95° (X10^3)
110° (X100)
125° (X10)
140°
• EXPERIMENT
□ COALESCENCE
E_c=10 MeV
P_o=170 MeV/c
--- COALESCENCE
E_c=0 MeV
P_o=197 MeV/c
$d^2N/N_f dE d\Omega$ (MeV · Sr)$^{-1}$
ENERGY (MEV)
10^7
10^6
10^5
10^4
10^3
100
10
1
0.1
10^{-2}
10^{-3}
10^{-4}
10^{-5}
10^{-6}
0
20
40
60
80
100

Fig. 24

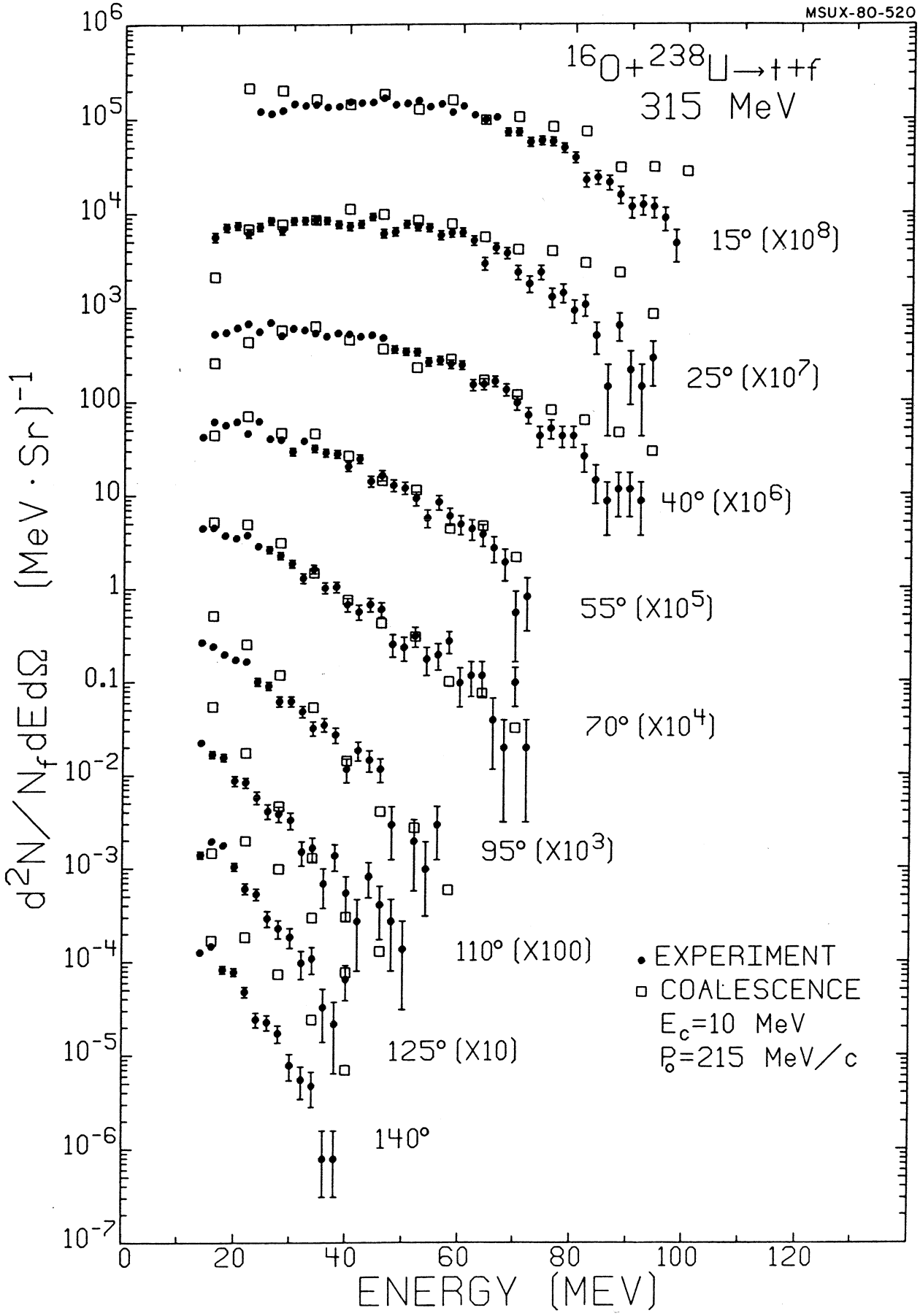
MSUX-80-520
$^{16}O+^{238}U \rightarrow t+f$
315 MeV
15° (X10^8)
25° (X10^7)
40° (X10^6)
55° (X10^5)
70° (X10^4)
95° (X10^3)
110° (X100)
125° (X10)
140°
• EXPERIMENT
□ COALESCENCE
E_c=10 MeV
P_o=215 MeV/c
$d^2N/N_f dE d\Omega$ (MeV · Sr)$^{-1}$
ENERGY (MEV)
10^6
10^5
10^4
10^3
100
10
1
0.1
10^{-2}
10^{-3}
10^{-4}
10^{-5}
10^{-6}
10^{-7}
0
20
40
60
80
100
120

Fig. 25

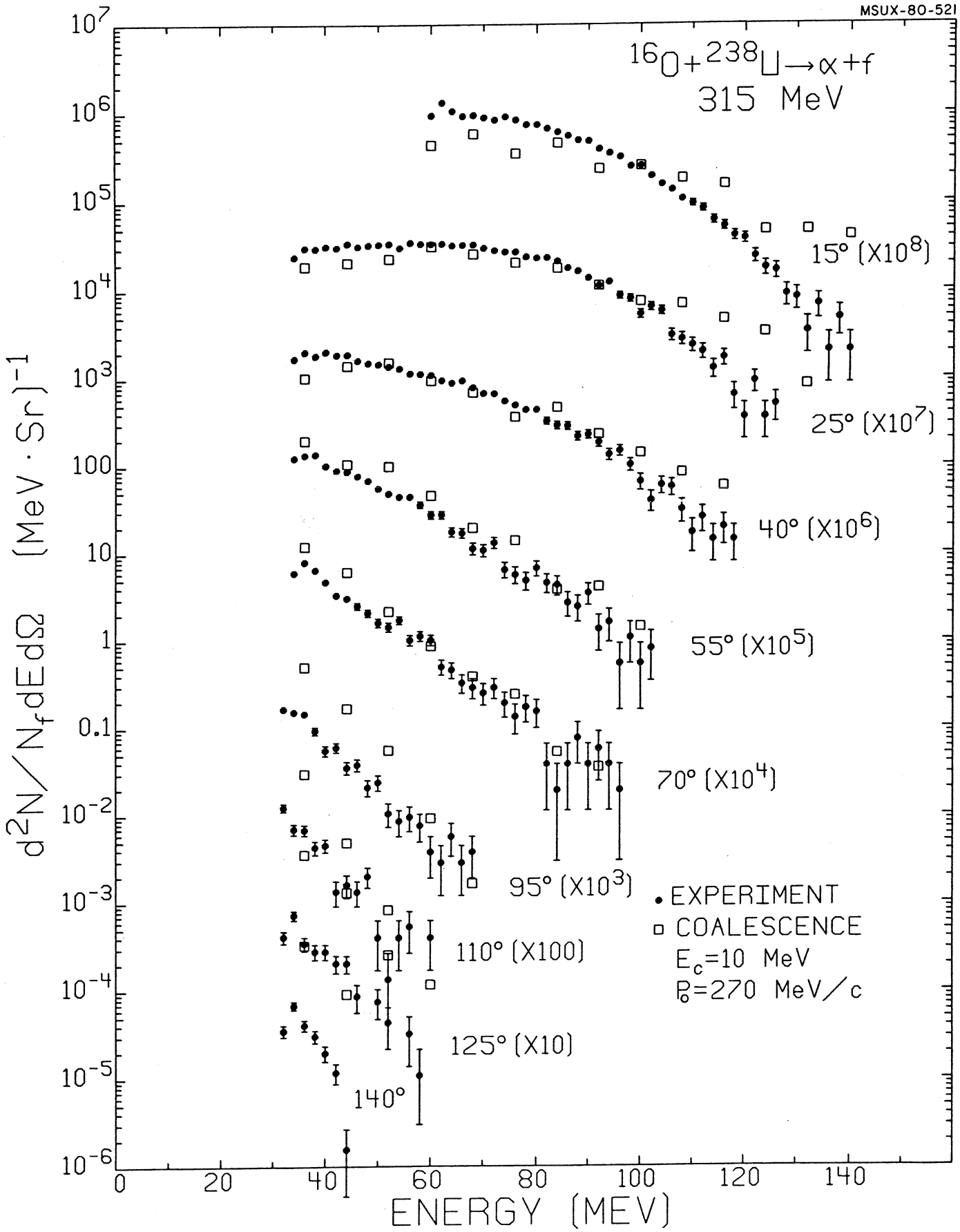
MSUX-80-521
$^{16}O + ^{238}U \rightarrow \alpha + f$
315 MeV
15° (X10^8)
25° (X10^7)
40° (X10^6)
55° (X10^5)
70° (X10^4)
95° (X10^3)
110° (X100)
125° (X10)
140°
• EXPERIMENT
□ COALESCENCE
E_c=10 MeV
P_o=270 MeV/c
$d^2N/N_f dE d\Omega$ (MeV · Sr)$^{-1}$
ENERGY (MEV)
10^7
10^6
10^5
10^4
10^3
100
10
1
0.1
10^{-2}
10^{-3}
10^{-4}
10^{-5}
10^{-6}
0
20
40
60
80
100
120
140

Fig. 26